Geometric Approaches to Motion Planning for Two Classes of Low Reynolds Number Swimmers

Jaskaran Singh Grover
CMU-RI-TR-18-37
July 27, 2018

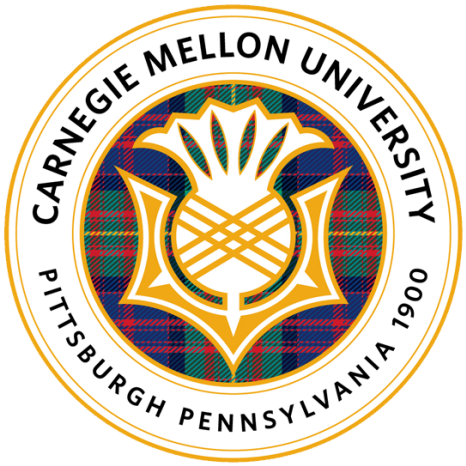

The Robotics Institute
School of Computer Science
Carnegie Mellon University
Pittsburgh, PA

Thesis Committee:
Professor Howie Choset
Professor Matthew Travers
Professor Scott David Kelly
Tony Dear

Submitted in partial fulfillment of the requirements
for the degree of
Master of Science in Robotics

Abstract

Microrobots have the potential to impact many areas of medicine such as microsurgery, targeted drug delivery and minimally invasive sensing. Just like microorganisms themselves, microrobots developed for these applications need to swim in a low-Reynolds number regime which warrants locomotive strategies that differ from their macroscopic counterparts. To this end, Purcell's three-link planar swimmer has served as an iconic model of a simple mechanism that can navigate this regime by leveraging internal actuation using analytically computed strokes [39]. We consider two different versions of this swimmer in this thesis. In the first class, we develop a novel three-dimensional counterpart to this swimmer and describe how enabling yaw-pitch movements at the two actuated joints as opposed to the conventional yaw-yaw movements allow it to navigate a three-dimensional environment. Using analytical tools from geometric mechanics, we design gaits that enable this swimmer to reorient itself and swim along canonical directions in the inertial frame. We validate these results on a hardware prototype and reproduce the simulated trajectories on the robot executing these gaits.

While the 3D swimmer is actuated internally, we next consider a second class of swimmers that are fabricated with elastomagnetic filaments and locomote in response to external magnetic fields. We demonstrate how the special case of a two link elastomagnetic swimmer is amenable for control synthesis using similar geometric arguments that apply to internally actuated swimmers. Additionally, we compute optimum internal magnetization distributions for a three-link swimmer that maximize its displacement per cycle and develop a principled approach to encode these distributions in millimeter-scale elastomagnetic filaments. We verify this procedure experimentally and finally demonstrate translation and turn-in-place locomotion in these swimmers.

Acknowledgements

I owe a huge debt of gratitude to my family and friends who have supported me over the last two years and kept me in high spirits which helped me in completing this thesis. First of all, I am thankful to my mother and my brother for being there every time and for teaching me how to embrace challenges with faith in God and with courage. I am grateful to my advisors Professor Choset, Dr. Travers and Professor Kelly for their feedback and constructive criticism as well as for supporting me over the last two years. Weekly meetings with Professor Kelly have involved delightful discussions on locomotion in fluids, control theory and geometry in addition to using correct grammar, vocabulary and several other topics which made Fridays the most awaited day of my week. Technical discussions with Tony have taught me valuable skills for approaching problems such as thinking patiently and developing the habit of intuitively understanding the rationale of complicated mathematical results. I am also thankful to Guillaume, Tony and Arun for their generous and kind support and for lending a helping hand that helped me navigate these two years with ease. I certainly cannot forget my *b*estie *a*mong *e*veryone Danny for his friendship, love, hard-work and for the power hugs and scares, I am lucky to call him my friend. I owe a great part of this thesis to Nalini, Patrick and Jake for their perseverance while conducting countless experiments, working hard and for creating a jolly work environment. I am so glad that I got the opportunity to work with with you all. I am also thankful to Chuck and Tim for teaching me how to handle tools in the machine shop and to Peggy and BJ for their support. Lastly, I want to thank everyone in the Biorobotics Lab for making me feel at home and for the lessons I learned working with them.

Contents

List of Tables

List of Figures

Chapter 1

Introduction

1.1 Overview

The term *locomotion* refers to the ability of a living creature or an autonomous robot to move from place to place. Biological organisms commonly employ periodic changes in their internal shape to achieve locomotion. The rectification of these periodic inputs coupled with interaction with the surrounding environment generates a net change in the position of the animal [28]. Such motions are observed at all scales in nature, for example, snakes propagate traveling waves along their length and exploit frictional contact with ground to advance forward [25]. Likewise, paramoecia employ periodic beating of hair-like cilia along their cell membrane to move forward [43]. These principles have also been exploited in mechanical systems to design *gaits i.e.* a sequence of periodic joint angle trajectories in the mechanism. For example, in [35], Murray and Sastry demonstrated the application of sinusoids to design velocity inputs for planning motions of car-like robots. The design of such gaits that perform a desired locomotory objective requires a physics-based model of the robot's interaction with its environment and tools from nonlinear control that harness this model and synthesize correct-by-construction motion plans.

Perhaps the earliest work employing these tools to locomotion of animals was that of Shapere and Wilczek who studied the movement of paramoecia in very low-Reynolds (Re) number regimes using ideas from gauge theory [28, 43]. While there has been significant work on understanding the motions of biological mircroorganisms in these regimes, more recently micro-swimming [31] has become a popular subject mainly because the progress in micro-manufacturing has made the fabrication of artificial microswimmers feasible [9, 36]. Such robotic microswimmers can have revolutionary impact for biomedical applications such as performing targeted drug delivery, microsurgery and minimally invasive diagnosis.

While mechanically designing systems at these small scales is challenging, there are also unanswered questions about how to control their movements, in particular, how to plan motions for robots that swim at low-Re numbers. In this thesis, we explore the problem of synthesizing motion primitives for two classes of artificial swimmers in this regime. The first swimmer is an internally actuated mechanism capable of swimming in a 3D environment with only two degrees of freedom. The ability to directly control both internal degrees of freedom (yaw and pitch) allows us to leverage existing geometric gait synthesis tools and extend their application to this novel prototype. Using tools from nonlinear control, we design translational and rotational primitives for this swimmer that allow it to turn in place and translate along its principal axes in the world. We implement these motion primitives on a robotic prototype and verify how translation in a 3D regime is possible using only two active inputs.

In the second class, we consider an externally actuated swimmer in which we relinquish

control over internal degrees of freedom. We focus on a millimeter scale elastomagnetic swimmer which undergoes deformations induced by time varying external magnetic fields that result in locomotion. This mechanism of swimming has been thoroughly studied in the literature as it offers an elegant and non-invasive method to drive devices without a wired connection, making it most suitable for microscopic locomotion. We investigate discrete planar swimmers consisting of uniformly magnetized links connected with passive revolute joints and springs. Using these models, we demonstrate how previous geometric arguments can be applied to the special case of a two link spring-less swimmer and can motivate previously proposed control laws. Secondly, building on [19], we use standard perturbation theoretic methods to analytically compute the internal magnetization distributions for a three link swimmer that maximize displacement per cycle of the actuating field. We also describe a principled approach to encode these distributions in millimeter scale elastomagnetic filaments which are used to fabricate swimmers. Finally, we verify results from numerical simulations by demonstrating locomotion in these swimmers in experiments using Helmholtz coils that generate time-varying magnetic fields.

1.2 Prior Work

In this work, we focus on artificial self-propelled swimmers whose mechanical designs and control, lend them the ability to navigate the low-Re regime. We provide a brief summary of related work in this area to give context. For the sake of convenience, we have divided the prior work in two sections. First we describe existing geometric and numerical tools for computing gaits for such swimmers and similar robots. We then describe existing magnetic microswimmers in the literature, their classification and modes of propulsion.

1.2.1 Geometric motion planning and optimal gait synthesis

In the low-Re regime, viscous forces dominate swimming and inertial effects are effectively negligible. Consequently, any forward momentum gained due to internal body deformations immediately ceases to exist when the body stops changing its shape, *i.e.* continuous movement requires continuous work [4]. Since Purcell's initial work on the three-link planar swimmer [39], much of the subsequent research has focused on planning motions and computing optimal gaits for the planar swimmer [44]. Hatton et. al. [23] demonstrate that using visual tools derived from geometric analysis, it is possible to synthesize gaits (cyclic changes in the internal shape) for the planar swimmer that make it move along a desired direction in the world. In addition to using numerical optimization for computing optimal gaits for these planar systems as in [6], authors in [45] use the minimum principle to derive efficient gaits. Furthermore, authors in [20] synthesize a novel suite of gaits for the classic three link swimmer by exploiting the symmetries in its velocities without leveraging curvature function techniques. Additionally, authors in [17] and [1] have developed analytical techniques to extend gait design to articulate systems with more than three links such as a snake like robot locomoting in granular media. While most of these systems have considered discrete models, authors in [10] consider a planar swimmer with a flexible tail and a load, and exploit curvature functions like tools (motility maps) to prescribe joint angles and joint angular velocities for actuation of these flagellar swimmers.

1.2.2 Magnetic microswimmers

In contrast to these works which mostly address motion planning for internally actuated systems, there has also been significant work on using external actuation to generate propulsion, specifically

using time varying magnetic fields. Typically in such systems, external magnetic fields create a torque on uniformly magnetized swimmers which respond to this field by undergoing shape deformations. [36] provides a comprehensive review on the state of the art in microswimmers.

There are three different types of magnetic microswimmers that currently exist. These include a swimmer made with a rigid helical tail which propels itself with a corkscrew like motion under the action of a rotating magnetic field. These swimmers rotate about their helical axis and translate in a direction perpendicular to the plane of rotation [16, 38, 42]. The second category consists of swimmers with flexible tails connected to a head as in [29, 26, 15]. Mathematical models for this type of swimmer have been developed in [14]. Under the action of an oscillating magnetic field, the magnetic head forces the flexible tail to wiggle in a non-reciprocal manner ultimately resulting in the net propulsion of the swimmer. The third category which is the focus of this thesis, consists of articulate swimmers made with discrete links attached to each other which undergo periodic planar undulations under the influence of crossed uniform and oscillating magnetic fields. We consider this swimmer because the elasticity provided by articulation inherently confers safety and locomotive efficiency to these swimmers at this scale. The mechanism of attaching links to each other is a design parameter. For example, authors in [13, 30] have considered attachment of strepatividin coated paramagnetic beads which bind to each other using elastic biotinilated DNA linkers. The corresponding elastic deformation models for these swimmers have been considered in [41] where the swimmer is modeled as an elastic beam. Similar swimmers and their dynamic models have been investigated using ferromagnetic filaments in [7, 5]. While these models are very accurate, they are not amenable to controller synthesis since they typically constitute a high-dimensional system state due to the continuum deformation of the flexible filaments. On the other end, authors in [27] developed a swimmer consisting of links connected to each other with flexible hinges. These swimmers can be modeled using a lumped parameter model which is suitable for motion planning and parametric optimization as explored in [18]. Moreover, the swimmer proposed in [19] consists of a non-magnetic spherical cargo connected to a rigid magnetic tail with a torsional spring. This model lies at the intersection of the swimmers in categories two and three above.

While all these swimmers are driven by magnetic torques induced by spatially uniform magnetic fields, it is also possible to induce displacement using spatially non-uniform magnetic fields which generate forces. Technically, force-induced locomotion cannot be termed swimming since the robot does not interact with the fluid to advance forward. Nevertheless, such gradient based actuation has been analytically proven to be less efficient in terms maximum achievable velocity compared to torque driven actuation for the specific case of a spherical head magnetic swimmer with a flexible tail. Authors in [38, 36] demonstrate analytically how controlling with field gradients is difficult as the force gradients decay faster with distance away from coils than field strengths.

1.3 Outline

The outline of this thesis is as follows:

In Chapter 2, we give a brief overview of low-Re locomotion and describe the derivation of the local connection for a planar three link swimmer. We dwell on how these equations of motion can be derived using velocities expressed in the world frame and velocities expressed in the body frame. This distinction is necessary because the mathematical model of the magnetic swimmer requires that the equations of motion be formulated with respect to world frame. We also give a brief overview of basic concepts from magnetism.

In Chapter 3, we extend the model of the planar swimmer to the internally actuated 3D

swimmer based on equations derived in Chapter 2. We numerically evaluate the controllability of this system and compute motion primitives using curvature functions. We describe the design of the 3D swimming robot and validate the motion primitives on this robot.

In Chapter 4, we investigate an externally actuated planar magnetic swimmer formed using uniformly magnetized links. We perform numerical simulations for a two link swimmer and a three link swimmer. For the three link swimmer, we use tools from perturbation theory to compute the optimum magnetization distribution for the links that maximizes displacement per cycle. We describe an approach to encode these constants in millimeter scale swimmers and validate results from numerical simulations experimentally.

In Chapter 5, we conclude this thesis and present directions for future work.

Chapter 2

Background

Locomotion at low- Reynolds regime (low-Re) is a very vast topic (See [32] for a detailed discussion). To keep the discussion brief, we focus here on modeling the dynamics of slender rigid bodies in low Re regimes which is a common theme in the coming chapters. We describe the forces and moments on a planar three link swimmer and derive the equations of motion using world frame velocities and body frame velocities. We briefly describe the effects of magnetic fields in terms of induced torques and forces.

2.1 Hydrodynamic forces and torques

Re is a characteristic non-dimensional parameter that is engendered by making Navier-Stokes' equations dimensionless. It is defined as:

$$Re = \frac{\rho u L}{\mu} = \frac{uL}{\nu} = \frac{f_{inertial}}{f_{viscous}} \tag{2.1}$$

It quantifies the relative magnitude of inertial forces to viscous forces on a body. It depends on the characteristic length of the body (L), velocity of the body (u), the density (ρ) of the fluid and the viscosity of the fluid (μ). Sometimes the parameter $\nu = \frac{\mu}{\rho}$ is called the kinematic viscosity. The motion in this regime is highly dampened by viscous forces and inertial effects are practically negligible. We now state the basic assumptions which will ultimately help us in deriving the equations of motion.

1. Each link in the swimmer is a slender rod, cylindrical in shape and neutrally buoyant. This assumption simplifies the analytical expressions for the viscous drag force and moment on each individual link.

2. The size of the swimmer is in the centimeter-scale range and the swimmer is completely submerged inside an enclosure filled with a highly viscous liquid. This is approximately hydrodynamically equivalent to a micro-scale swimmer submerged in a less viscous liquid like water. We make this assumption because the resulting Re at this size to viscosity ratio falls in the low-Re number regime.

3. The enclosure containing the fluid does not have any walls. The absence of walls decouples the motion of the swimmer from boundary effects.

4. Likewise, in the case of a three-link swimmer, the motion of one link does not effect the motion of another link *i.e.*, the links are hydrodynamically isolated from one another.

With these assumptions, we can now analyze the constraints imposed due to interaction with the surrounding medium. Swimming in the low-*Re* number regime imposes what are known as *nonholonomic constraints* on the swimmer's velocity. These constraints *approximately* indicate the directions in which the swimmer is forbidden to move. These are as follows:

1. The resistive force theory (RFT) states that the drag force acting on a slender body in a viscous medium is directly proportional to its velocity. The faster the swimmer tries to change its internal shape, the greater is the amount of damping.

2. Secondly, the net drag force on an isolated system interacting with a viscous liquid vanishes, *i.e.* the swimmer is always in a state of quasistatic equilibrium.

3. Finally, viscous forces (and moments) in the lateral directions are twice as large as those in the longitudinal direction, *i.e.*, it is twice as difficult to move along any of the lateral axes as it is to move along the longitudinal axis.

2.1.1 Equations of motion (body frame):

Consider a three link swimmer as shown in Figure. 2.1. The body frame of link i is attached rigidly to the center of the link as shown in the figure and is denoted as $\{x_b^i, y_b^i\}$ for $i \in \{1, 2, 3\}$. The body velocity of link i is denoted by $\boldsymbol{\xi_i}$, where $\boldsymbol{\xi_i} = (\xi_x, \xi_y, \xi_{\theta_x})_i$ and $i \in \{1, 2, 3\}$ corresponding to the three links. The body velocity represents the velocity of a body fixed frame that is measured relative to the inertial frame but expressed in the body frame. The drag force relative to the body frame $\boldsymbol{F_i^b}$ (superscript $\boldsymbol{b}$ is for body-frame) and drag torque relative to the body frame $\boldsymbol{\tau_i^b}$ on link i are collectively denoted by a wrench

$$\mathbf{W}_i = \begin{bmatrix} \boldsymbol{F_i^b} & \boldsymbol{\tau_i^b} \end{bmatrix} \in T_g^* G \tag{2.2}$$

which according to RFT is defined as

$$\mathbf{W}_i = K \boldsymbol{\xi_i}, \tag{2.3}$$

where

$$K = \begin{bmatrix} k_T L & 0 & 0 \\ 0 & 2k_T L & 0 \\ 0 & 0 & \frac{2}{3} k_T L^3 \end{bmatrix}. \tag{2.4}$$

Here k_T is the viscous drag coefficient that depends on the length and radii of the links and viscosity of the medium. It is assumed that all three links are identical in geometry so that the drag matrix K is identical for all three of them. We are interested in tracking the position and orientation of the reference link (link 2) of the swimmer. It is therefore desirable to express the body velocities of links 1 and 3 as a function of the body velocity of the reference link. We use standard relations from [34]

$$\boldsymbol{\xi_1} = \underbrace{\begin{bmatrix} \cos\alpha_1 & \sin\alpha_1 & -\frac{L}{2}\sin\alpha_1 \\ -\sin\alpha_1 & \cos\alpha_1 & \frac{L}{2}(1+\cos\alpha_1) \\ 0 & 0 & 1 \end{bmatrix}}_{M_1} \boldsymbol{\xi_2} + \underbrace{\begin{bmatrix} 0 \\ \frac{L}{2} \\ -1 \end{bmatrix}}_{J_1} \dot{\alpha}_1 \tag{2.5}$$

$$= M_1 \boldsymbol{\xi_2} + J_1 \dot{\alpha}_1 \tag{2.6}$$

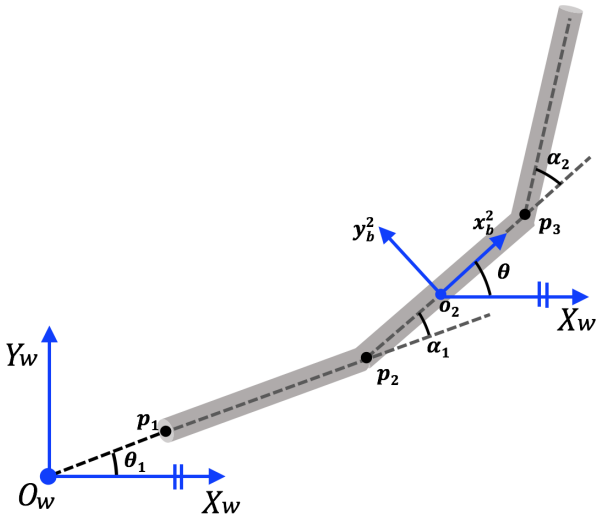

Figure 2.1: Top view of the three link planar swimmer

$$\boldsymbol{\xi_3} = \underbrace{\begin{bmatrix} \cos\alpha_2 & \sin\alpha_2 & \frac{L}{2}\sin\alpha_2 \\ -\sin\alpha_2 & \cos\alpha_2 & \frac{L}{2}(1+\cos\alpha_1) \\ 0 & 0 & 1 \end{bmatrix}}_{M_2} \boldsymbol{\xi_2} + \underbrace{\begin{bmatrix} 0 \\ \frac{L}{2} \\ 1 \end{bmatrix}}_{J_2} \dot{\alpha}_2 \tag{2.7}$$

$$= M_2\boldsymbol{\xi_2} + J_2\dot{\alpha}_2 \tag{2.8}$$

Likewise, we can also express the forces expressed in the body frames of links 1 and 3 (Eq. 2.3) respectively relative to the body frame of link 2. This is necessary because we eventually want to write the net wrench on the system which requires that all individual forces be expressed in the same frame.

$$\tilde{\boldsymbol{W}}_\mathbf{1} = M_1^T\boldsymbol{W_1} = M_1^T K\boldsymbol{\xi_1} \tag{2.9}$$

$$\tilde{\boldsymbol{W}}_\mathbf{3} = M_2^T\boldsymbol{W_3} = M_2^T K\boldsymbol{\xi_3} \tag{2.10}$$

Finally from the quasistatic equilibrium constraint, we get:

$$\begin{aligned}
&\tilde{\boldsymbol{W}}_\mathbf{1} + \boldsymbol{W_2} + \tilde{\boldsymbol{W}}_\mathbf{3} = 0 \\
\implies & M_1^T K\boldsymbol{\xi_1} + K\boldsymbol{\xi_2} + M_2^T K\boldsymbol{\xi_3} = 0 \\
\implies & M_1^T K(M_1\boldsymbol{\xi_2} + J_1\dot{\alpha}_1) + K\boldsymbol{\xi_2} + M_2^T K(M_2\boldsymbol{\xi_2} + J_2\dot{\alpha}_2) = 0 \\
\implies & (M_1^T K M_1 + K + M_2^T K M_2)\boldsymbol{\xi_2} + \begin{bmatrix} M_1^T K J_1 & M_2^T K J_2 \end{bmatrix}\dot{\boldsymbol{\alpha}} = 0 \\
\implies & \omega_\xi\boldsymbol{\xi_2} + \omega_\alpha\dot{\boldsymbol{\alpha}} = 0 \\
\implies & \boldsymbol{\xi_2} = -\omega_\xi^{-1}\omega_\alpha\dot{\boldsymbol{\alpha}} \\
\implies & \boldsymbol{\xi_2} = -A(\boldsymbol{\alpha})\dot{\boldsymbol{\alpha}}
\end{aligned} \tag{2.11}$$

where $A(\boldsymbol{\alpha}) \in \mathbb{R}^{3\times 2}$ is known as the local form of connection, which maps shape velocities to body velocities *i.e.* $A(\boldsymbol{\alpha}) : T_{\alpha_1}S^1 \times T_{\alpha_2}S^1 \longrightarrow \mathfrak{se}(2)$. Eq. 2.11 is known as the *Kinematic Reconstruction Equation* which relates changes in the internal shape of the planar swimmer to its body velocity. We will now derive this same equation by analyzing the forces on the swimmer measured directly relative to the world frame.

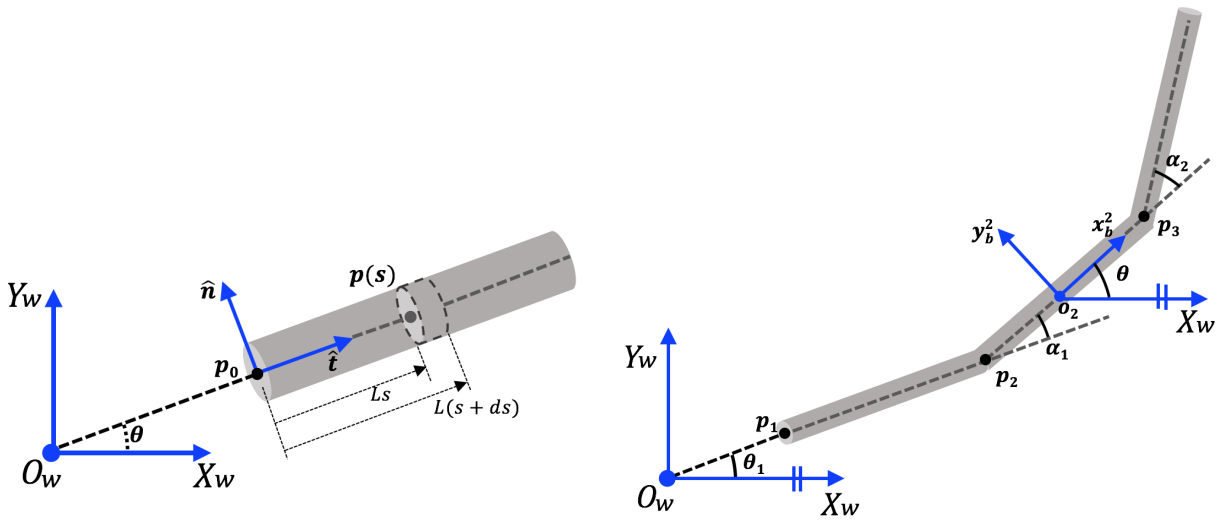

(a) Top view of a single link for world calculations (b) Top view of the three-link planar swimmer

Figure 2.2: Hydrodynamic drag forces and torques on a single link and the three-link swimmer

2.1.2 Equations of motion (world frame)

We now analyze forces and moments on each individual link relative to the world frame. Refer to Figure. 2.2a. Let $\boldsymbol{v}_0 = \dot{\boldsymbol{p}}_0$ denote the velocity of the point $\boldsymbol{p}_0$ expressed relative to the world frame W. From the assumptions of resistive force theory, we know that the drag force per unit length on this slender link depends linearly on its velocity. We will use these assumptions to compute the net hydrodynamic drag force and the associated torque as a function of the swimmer's velocity.

Drag Force

Let $s \in [0, 1]$ denote the arc length parameter that sweeps along the length of the link. Using this representation, any point along the longitudinal axis of the link can be represented using

$$\boldsymbol{p}(s) = \boldsymbol{p}_0 + sL\hat{\boldsymbol{t}} \tag{2.12}$$

where $\hat{\boldsymbol{t}}$ is the unit vector along the tangent/longitudinal axis of the link and is given by $\hat{\boldsymbol{t}} = (\cos\theta, \sin\theta)$. Similarly, $\hat{\boldsymbol{n}}$ is the unit vector along the normal/lateral axis of the link and is given by $\hat{\boldsymbol{n}} = (-\sin\theta, \cos\theta)$. The velocity of each point on the link can be computed by differentiating Eq. 2.12 giving Eq. 2.13

$$\dot{\boldsymbol{p}}(s) = \dot{\boldsymbol{p}}_0 + sL\hat{\boldsymbol{n}}\dot{\theta} \tag{2.13}$$

because $\frac{d\hat{\boldsymbol{t}}}{dt} = \hat{\boldsymbol{n}}\dot{\theta}$. The hydrodynamic force per unit length is given by

$$\boldsymbol{f}_{p.u.l}(s) = -c_t\langle\dot{\boldsymbol{p}}(s), \hat{\boldsymbol{t}}\rangle\hat{\boldsymbol{t}} - c_n\langle\dot{\boldsymbol{p}}(s), \hat{\boldsymbol{n}}\rangle\hat{\boldsymbol{n}} \tag{2.14}$$

where c_n, c_t are the lateral and longitudinal drag coefficients respectively. They are related by $c_n = 2c_t = 2k_T$. By substituting Eq. 2.13 in Eq. 2.14, we get

$$\boldsymbol{f}_{p.u.l}(s) = -c_t\langle\dot{\boldsymbol{p}}_0 + sL\hat{\boldsymbol{n}}\dot{\theta}, \hat{\boldsymbol{t}}\rangle\hat{\boldsymbol{t}} - c_n\langle\dot{\boldsymbol{p}}_0 + sL\hat{\boldsymbol{n}}\dot{\theta}, \hat{\boldsymbol{n}}\rangle\hat{\boldsymbol{n}} \tag{2.15}$$

$$= -c_t\langle\dot{\boldsymbol{p}}_0, \hat{\boldsymbol{t}}\rangle\hat{\boldsymbol{t}} - c_n\langle\dot{\boldsymbol{p}}_0, \hat{\boldsymbol{n}}\rangle\hat{\boldsymbol{n}} - c_n sL\dot{\theta}\hat{\boldsymbol{n}} \tag{2.16}$$

The total force on a patch between points parameterized by $L(s+ds)$ and Ls is given by

$$\boldsymbol{F}_{patch} = \boldsymbol{f}_{p.u.l}(s)\Big(L(s+ds) - Ls\Big) \tag{2.17}$$

The net hydrodynamic force is obtained by integrating Eq. 2.17 over the length of the link

$$\begin{aligned}
\boldsymbol{F}_h &= \int_0^1 \boldsymbol{F}_{patch} \\
&= L\int_0^1 \boldsymbol{f}_{p.u.l}(s)ds \\
&= -c_t L\langle \dot{\boldsymbol{p}}_0, \hat{\boldsymbol{t}}\rangle \hat{\boldsymbol{t}} - c_n L\langle \dot{\boldsymbol{p}}_0, \hat{\boldsymbol{n}}\rangle \hat{\boldsymbol{n}} - \frac{L^2}{2}\dot{\theta}\hat{\boldsymbol{n}}
\end{aligned} \tag{2.18}$$

Drag Torque

We will now compute the net drag torque on the link about an arbitrary point $\boldsymbol{x}_0$. This torque arises due to the resistance of the fluid to the link's rotation. Using the expression for the drag force per unit length from Eq. 2.14, we compute the torque per unit length below

$$\begin{aligned}
\boldsymbol{\tau}_{p.u.l}^{\boldsymbol{x}_0}(s) &= (\boldsymbol{p}(s) - \boldsymbol{x}_0) \times \boldsymbol{f}_{p.u.l}(s) \\
&= (\boldsymbol{p}_0 + sL\hat{\boldsymbol{t}} - \boldsymbol{x}_0) \times \boldsymbol{f}_{p.u.l}(s) \\
&= (\boldsymbol{p}_0 - \boldsymbol{x}_0) \times \boldsymbol{f}_{p.u.l}(s) + sL\hat{\boldsymbol{t}} \times \boldsymbol{f}_{p.u.l}(s)
\end{aligned} \tag{2.19}$$

The net torque is thus given by integrating this torque per unit length over a patch of length Lds

$$\begin{aligned}
\boldsymbol{\tau}_h^{\boldsymbol{x}_0} &= \int_0^1 \boldsymbol{\tau}_{p.u.l}^{\boldsymbol{x}_0}(s) L ds \\
&= \int_0^1 \Big((\boldsymbol{p}_0 - \boldsymbol{x}_0) \times \boldsymbol{f}_{p.u.l}(s) + sL\hat{\boldsymbol{t}} \times \boldsymbol{f}_{p.u.l}(s)\Big) Lds \\
&= L\int_0^1 \Big((\boldsymbol{p}_0 - \boldsymbol{x}_0) \times \boldsymbol{f}_{p.u.l}(s)\Big) ds + L^2 \int_0^1 \Big(s\hat{\boldsymbol{t}} \times \boldsymbol{f}_{p.u.l}(s)\Big) ds \\
&= \Bigg((\boldsymbol{p}_0 - \boldsymbol{x}_0) \times \underbrace{L\int_0^1 \boldsymbol{f}_{p.u.l}(s)ds}_{\boldsymbol{F}_h}\Bigg) - c_n L^2 \Bigg(\langle \dot{\boldsymbol{p}}_0, \hat{\boldsymbol{n}}\rangle \int_0^1 sds + L\dot{\theta}\int_0^1 s^2 ds\Bigg)\hat{\boldsymbol{e}}_z \\
&= \Big((\boldsymbol{p}_0 - \boldsymbol{x}_0) \times \boldsymbol{F}_h\Big) - c_n\Big(\frac{L^2}{2}\langle \dot{\boldsymbol{p}}_0, \hat{\boldsymbol{n}}\rangle + \frac{L^3}{3}\dot{\theta}\Big)\hat{\boldsymbol{e}}_z
\end{aligned} \tag{2.20}$$

Now, refer to Figure 2.2b, using these expressions for the force and torque on a single link, we can write the quasi-static equilibrium condition for the three link swimmer as:

$$\begin{aligned}
\boldsymbol{F}_{1,h} + \boldsymbol{F}_{2,h} + \boldsymbol{F}_{3,h} &= 0 \\
\hat{\boldsymbol{e}}_z \cdot (\boldsymbol{\tau}_{1,h}^{\boldsymbol{p}_1} + \boldsymbol{\tau}_{2,h}^{\boldsymbol{p}_1} + \boldsymbol{\tau}_{3,h}^{\boldsymbol{p}_1}) &= 0
\end{aligned} \tag{2.21}$$

where $\hat{\boldsymbol{e}}_z = (0, 0, 1)^T$. In order to reference all the hydrodynamic forces and torques relative to $\boldsymbol{o_2}$ (see Figure 2.2b), we use

$$\begin{aligned}
\dot{\boldsymbol{p}}_2 &= \dot{\boldsymbol{o}}_2 - \frac{L}{2}\hat{\boldsymbol{n}}_2\dot{\theta} \\
\dot{\boldsymbol{p}}_1 &= \dot{\boldsymbol{p}}_2 - L\hat{\boldsymbol{n}}_1\dot{\theta}_1 = \dot{\boldsymbol{p}}_2 - L\hat{\boldsymbol{n}}_1(\dot{\theta} - \dot{\alpha}_1) = \dot{\boldsymbol{o}}_2 - \frac{L}{2}\hat{\boldsymbol{n}}_2\dot{\theta} - L\hat{\boldsymbol{n}}_1(\dot{\theta} - \dot{\alpha}_1) \\
\dot{\boldsymbol{p}}_3 &= \dot{\boldsymbol{p}}_2 + L\hat{\boldsymbol{n}}_2\dot{\theta} = \dot{\boldsymbol{o}}_2 - \frac{L}{2}\hat{\boldsymbol{n}}_2\dot{\theta} + L\hat{\boldsymbol{n}}_2\dot{\theta}
\end{aligned} \tag{2.22}$$

Finally substituting $\dot{\boldsymbol{o}}_2 = R_{-\theta}\boldsymbol{\xi}$ in Eq. 2.22 and substituting Eqs. 2.22, 2.18 and 2.20 in Eq. 2.21 gives the desired result.

2.2 Magnetic forces and torques

The basic principle of actuation using magnetic fields is to apply either a magnetic force or a magnetic torque. Magnetic forces arise due to spatial gradients of the magnetic field whereas magnetic torques arise due to misalignment of the internal moments of the magnetic links relative to the external magnetic field. Figure 2.3 shows the top view of a slender magnetic link. Point $\boldsymbol{p}_0$ denotes the origin of the body frame attached rigidly to the tip of the link with respect to O, the origin of the (X_w, Y_w) plane. The longitudinal axis of the body frame is denoted by $\hat{\boldsymbol{t}}$ and the lateral axis of the body frame is denoted by $\hat{\boldsymbol{n}}$. In the given representation, it is easy to see that $\hat{\boldsymbol{t}} = (\cos\theta, \sin\theta)$ and $\hat{\boldsymbol{n}} = (-\sin\theta, \cos\theta)$. The entire plane is under the influence of a magnetic field $\boldsymbol{B}(\boldsymbol{x}, t) = (B_x(\boldsymbol{x}, t), B_y(\boldsymbol{x}, t))$ where B_x denotes the horizontal (along X_w) component of the spatial magnetic field $\boldsymbol{B}(\boldsymbol{x}, t)$ and likewise B_y denotes the vertical (along Y_w) component of the spatial magnetic field. In the current form, the magnetic field vector at a given point $\boldsymbol{x}$ depends on the position of the point with respect to O_w as well as on time t.

Forces due to spatial gradients:

Given a spatial magnetic field denoted as $\boldsymbol{B}(\boldsymbol{x}, t) = (B_x(\boldsymbol{x}, t), B_y(\boldsymbol{x}, t))$, the jacobian of this field is defined as:

$$\nabla\boldsymbol{B}(\boldsymbol{x}, t) = \begin{pmatrix} \frac{\partial B_x(\boldsymbol{x},t)}{\partial x} & \frac{\partial B_x(\boldsymbol{x},t)}{\partial y} \\ \frac{\partial B_y(\boldsymbol{x},t)}{\partial x} & \frac{\partial B_y(\boldsymbol{x},t)}{\partial y} \end{pmatrix} \tag{2.23}$$

The internal magnetization of a link is expressed relative to the body frame that is rigidly attached to the link as shown in Figure 2.3. It has components along the longitudinal axis as well as along the lateral axis of the link given by $m_t h$ and $m_n h$ respectively. Relative to the local body frame, the magnetization of the link can be written as $\boldsymbol{M^b} = (m_t h, m_n h)$ where the first component is along $\hat{\boldsymbol{t}}$ and the second component is along $\hat{\boldsymbol{n}}$. On the other hand, relative to the world frame W, the magnetization of the link can be written as:

$$\begin{aligned}
\boldsymbol{M^w} &= (m_t\hat{\boldsymbol{t}} + m_n\hat{\boldsymbol{n}})h \\
&= (m_t\cos\theta - m_n\sin\theta, m_t\sin\theta + m_n\cos\theta)h
\end{aligned} \tag{2.24}$$

where $m_t \in [-1, 1]$ and $m_n \in [-1, 1]$ are dimensionless numbers. $h > 0$ is the actual internal magnetization with units Am^{-1}. The splitting of individual components into a dimensionless number and a base value h is done to ensure that the behavior of the swimmer as a function of external magnetic fields and internal magnetizations (Section 4.3) can be described qualitatively

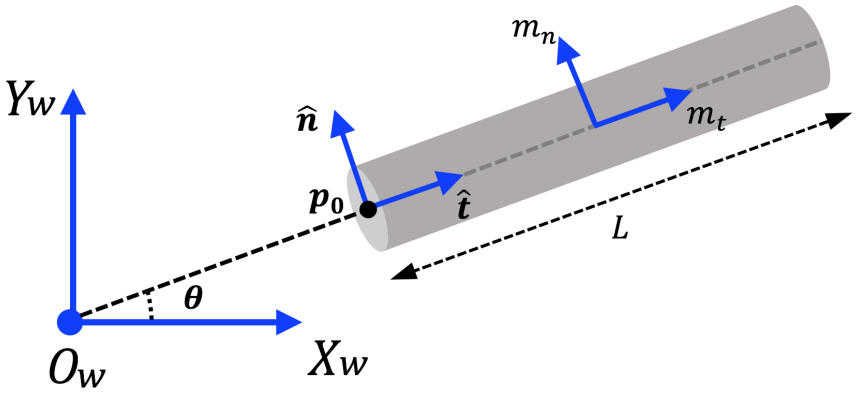

Figure 2.3: Illustration of a single magnetic link in a low-Re regime. m_t and m_n denote the tangential and normal components of internal magnetization

using dimensionless parameters. Additionally, we assume that the link is made up of a ferromagnetic material, which makes h independent of the external actuating field. This is not true in the case of a paramagnetic material. From this point onwards, we will always assume that magnetizations are expressed relative to the world frame while still respecting that they are intrinsically defined with respect to the body frame. Given a magnetic link with volume V and internal magnetization $\boldsymbol{M}$ ($=\boldsymbol{M}^{\boldsymbol{w}}$), one can compute the total magnetic force on the link using

$$\boldsymbol{F}_{mag} = V\boldsymbol{M} \cdot \nabla \boldsymbol{B}(\boldsymbol{x}, t) \tag{2.25}$$

In the case where the magnetic field is spatially uniform *i.e.* $\nabla \boldsymbol{B}(\boldsymbol{x}, t) = 0$, there is no magnetic force on the link. Such a field is generated by a pair of equal current carrying coils facing each other in the Helmholtz configuration [40].

Torques due to misalignment:

The potential energy stored in a link due to misalignment of its internal magnetization relative to the external magnetic field is defined as

$$U = -V\boldsymbol{M} \cdot \boldsymbol{B}(\boldsymbol{x}, t) \tag{2.26}$$

This stored potential energy is analogous to the energy stored in a deformed linear spring. Just like the spring, the natural tendency of an unhinged magnet is to align itself with the external magnetic field until the stored energy is minimized. This motion is facilitated by a torque exerted by the external magnetic field on the link. This restoring torque is computed using

$$\boldsymbol{\tau}_{mag} = V\boldsymbol{M} \times \boldsymbol{B}(\boldsymbol{x}, t) \tag{2.27}$$

Note here that if the magnetic field is spatially uniform *i.e.* it varies only in time but not in space, then the magnetic torque will not vanish *i.e.* $\boldsymbol{\tau}_{mag} = V\boldsymbol{M} \times \boldsymbol{B}(t) \neq 0$ even though the force does. In the rest of the chapter, we assume that the swimmer is placed in a region of spatially uniform magnetic field. Since the field and the motion of the swimmer are restricted to the $\{X_w, Y_w\}$ plane, the magnetic torque acts about the Z_w axis only and can simply be written as a scalar given by $\tau_{mag} = Vh\big(B_y(t)(m_t \cos\theta - m_n \sin\theta) - B_x(t)(m_t \sin\theta + m_n \cos\theta)\big)$ using Eq. 2.24 in Eq. 2.27.

2.3 Summary

In this chapter, we derived expressions for the hydrodynamic drag force and hydrodynamic drag torque on slender rigid bodies using calculations in the body frame and the world frame. This distinction will be useful when deriving the equations of motion for the 3D swimmer and the magnetic swimmer. In particular, since the 3D swimmer is internally actuated, local body frame calculations are more revealing and directly lead to the formulation of the kinematic reconstruction equation. Hence, the derivation for the equations of motion for 3D swimmer in the Chapter 3 will be more akin to the derivation for the planar swimmer in this chapter. On the other hand, since the moments on the magnetic swimmer depend on its orientation relative to the world, it becomes necessary to write the equations relative to the world frame. This will be described in Chapter 4.

Chapter 3

Internally actuated 3D Swimmer

3.1 Introduction

As mentioned in the introduction, we consider a 3D swimmer which is closely related to the classic planar swimmer. In our design, we allow for out-of-plane motions in the swimmer using yaw and pitch control of two non-coplanar revolute joints in contrast to only yaw-yaw type motions of the planar swimmer. We test the hypothesis of being able to reach any position and assume any orientation in 3D space using the test of small time local controllability, the Chow-Rashevsky theorem [34]. For this test, we study the kinematics of swimming in this regime, derive a mathematical model and investigate how direct command over the internal degrees of freedom can be used to control the position and orientation of the 3D swimmer in the world, eventually paving the way for motion planning in a 3D regime.

The rest of the chapter is organized as follows: In Section 3.2, we describe the mathematical model of the 3D swimmer and derive the equations of motion based on resistive force theory [11]. In Section 3.3, we demonstrate empirically that the kinematic model of the swimmer is small time locally controllable, *i.e.* we can synthesize control inputs that can steer the swimmer between any two arbitrary configurations in the world. In Section 3.4, we derive gaits for steering the swimmer along a desired direction in the world frame using connection curvature functions. In Section 3.5, we show experimental results on a robotic swimmer and finally in Section 3.6, we present conclusions and directions for future work.

3.2 Mathematical Model

3.2.1 Configuration Space

The 3D swimmer consists of three links connected by two revolute joints, where the axes of rotation of the two joints are orthogonal. As shown in Fig. 3.1, joint one admits motion in the body yaw direction which is parameterized by α_1 and joint two admits motion in the body pitch direction which is parametrized by α_2. Each of the three links has length L and is considered to be slender, as required by resistive force theory [11].

The configuration space Q of any locomoting system such as the 3D swimmer, can generally be split into a position space G and an internal shape space M, *i.e.*, $Q = G \times M$ [37]. Any element $g \in G$, where in our case $G = SE(3)$, represents the position and orientation of the body frame of the swimmer with respect to the world frame. The internal shape space $M = S^1 \times S^1$ is characterized by angles α_1 and α_2. With this natural splitting, we now derive a kinematic expression that relates changes in the internal shape of the swimmer to its motion in the inertial

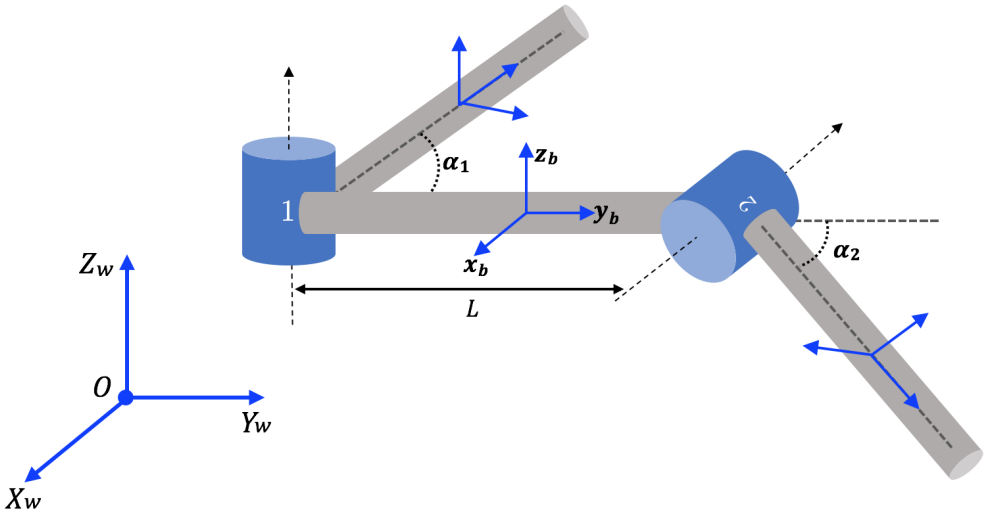

Figure 3.1: 3D Swimmer Schematic

frame. In the following sections, we assume that the swimmer has a frame which is rigidly attached to the center of the middle link as shown in Fig. 3.1. We will be interested in analyzing the motion of this body fixed frame through the rest of the paper.

3.2.2 Equations of Motion

We refer the reader to Section 2.1 for a brief review on the derivation of forces and moments on slender rods submerged in viscous media. The derivation of the equations of motion for the 3D swimmer is very similar to one for the planar swimmer presented in Section 2.1. The body velocity of link i is denoted by $\boldsymbol{\xi_i}$, where $\boldsymbol{\xi_i}= (\xi_x, \xi_y, \xi_z, \xi_{\theta_x}, \xi_{\theta_y}, \xi_{\theta_z})_i$ and $i \in \{1, 2, 3\}$ corresponding to each link. The body velocity denotes the velocity of a body-fixed frame measured relative to the inertial frame and expressed in the body frame. The drag force $\boldsymbol{F_i^b}$ and drag torque $\boldsymbol{\tau_i^b}$ on link i are collectively denoted by a wrench

$$\mathbf{W}_i = \begin{bmatrix} \boldsymbol{F_i^b} & \boldsymbol{\tau_i^b} \end{bmatrix} \in T_g^* G \tag{3.1}$$

which according to RFT is defined as

$$\mathbf{W}_i = K\boldsymbol{\xi_i}, \tag{3.2}$$

where

$$K = \begin{bmatrix} 2k_T L & 0 & 0 & 0 & 0 & 0 \\ 0 & k_T L & 0 & 0 & 0 & 0 \\ 0 & 0 & 2k_T L & 0 & 0 & 0 \\ 0 & 0 & 0 & \frac{2}{3}k_R L^3 & 0 & 0 \\ 0 & 0 & 0 & 0 & \frac{1}{3}k_R L^3 & 0 \\ 0 & 0 & 0 & 0 & 0 & \frac{2}{3}k_R L^3 \end{bmatrix}. \tag{3.3}$$

Here, k_R and k_T are the rotational and translational viscous drag coefficients respectively that depend on the length and radii of the links. It is assumed that all three links are identical in

geometry so that the drag matrix K is identical for all three of them. We identify the motion of the swimmer with the position and orientation of the reference link *i.e.* link 2 of the swimmer. It is therefore desirable to express the body velocities of links 1 and 3 as a function of the body velocity of the reference link. We use standard relations from [34]:

$$\boldsymbol{\xi_1} = Ad_{g_{L_2L_1}^{-1}} \boldsymbol{\xi_2} + \boldsymbol{\xi}_{\boldsymbol{L_2L_1}}^{\boldsymbol{L_2}} \tag{3.4}$$

$$\boldsymbol{\xi_3} = Ad_{g_{L_2L_3}^{-1}} \boldsymbol{\xi_2} + \boldsymbol{\xi}_{\boldsymbol{L_2L_3}}^{\boldsymbol{L_2}} \tag{3.5}$$

Here

$$\boldsymbol{\xi}_{\boldsymbol{L_2L_1}}^{\boldsymbol{L_2}} = (-\tfrac{L}{2} \quad 0 \quad 0 \quad 0 \quad 0 \quad 1)^T \dot{\alpha}_1 = \boldsymbol{J_1}\dot{\alpha}_1, \tag{3.6}$$

$$\boldsymbol{\xi}_{\boldsymbol{L_2L_3}}^{\boldsymbol{L_2}} = (0 \quad 0 \quad \tfrac{L}{2} \quad -1 \quad 0 \quad 0)^T \dot{\alpha}_2 = \boldsymbol{J_3}\dot{\alpha}_2. \tag{3.7}$$

where $Ad_g : \mathfrak{se}(3) \longrightarrow \mathfrak{se}(3)$ maps body velocity twists to spatial velocity twists. $\mathfrak{se}(3)$ is the Lie algebra for the Lie group $SE(3)$. $g_{L_2L_1}$ represents the relative transformation between the body frame of link 1 and link 2 and similarly $g_{L_2L_3}$ represents the relative transformation between the body frame of link 3 and link 2. $\boldsymbol{\xi}_{\boldsymbol{L_2L_1}}^{\boldsymbol{L_2}}$ is the body velocity of link 1 relative to link 2 and expressed in link 2's reference frame. Similarly, $\boldsymbol{\xi}_{\boldsymbol{L_2L_3}}^{\boldsymbol{L_2}}$ is the body velocity of link 3 relative to link 2 and expressed in link 2's reference frame. We can rewrite the wrenches $\mathbf{W}_1$ and $\mathbf{W}_3$ in terms of a wrench applied at the origin of the body frame and with respect to the body frame using

$$\tilde{\mathbf{W}}_1 = Ad^T_{g_{L_2L_1}^{-1}} \mathbf{W}_1 = Ad^T_{g_{L_2L_1}^{-1}} K\boldsymbol{\xi_1} = Ad^T_{g_{L_2L_1}^{-1}} K\big(Ad_{g_{L_2L_1}^{-1}} \boldsymbol{\xi_2} + \boldsymbol{\xi}_{\boldsymbol{L_2L_1}}^{\boldsymbol{L_2}}\big) \tag{3.8}$$

$$\tilde{\mathbf{W}}_3 = Ad^T_{g_{L_2L_3}^{-1}} \mathbf{W}_3 = Ad^T_{g_{L_2L_3}^{-1}} K\boldsymbol{\xi_3} = Ad^T_{g_{L_2L_3}^{-1}} K\big(Ad_{g_{L_2L_3}^{-1}} \boldsymbol{\xi_2} + \boldsymbol{\xi}_{\boldsymbol{L_2L_3}}^{\boldsymbol{L_2}}\big) \tag{3.9}$$

From the quasistatic equilibrium assumption, we know that the net force and moment on the swimmer vanishes, *i.e.*,

$$\begin{aligned}
&\tilde{\mathbf{W}}_1 + \mathbf{W}_2 + \tilde{\mathbf{W}}_3 = \mathbf{0} \\
\implies &Ad^T_{g_{L_2L_1}^{-1}} \mathbf{W}_1 + \mathbf{W}_2 + Ad^T_{g_{L_2L_3}^{-1}} \mathbf{W}_3 = \mathbf{0} \\
\implies &\underbrace{\big(Ad^T_{g_{L_2L_1}^{-1}} KAd_{g_{L_2L_1}^{-1}} + K + Ad^T_{g_{L_2L_3}^{-1}} KAd_{g_{L_2L_3}^{-1}}\big)}_{\omega_\xi} \boldsymbol{\xi_2} + \underbrace{\big(Ad^T_{g_{L_2L_1}^{-1}} KJ_1 + Ad^T_{g_{L_2L_3}^{-1}} KJ_3\big)}_{\omega_\alpha} \dot{\boldsymbol{\alpha}} = \mathbf{0} \\
\implies &\omega_\xi \boldsymbol{\xi_2} + \omega_\alpha \dot{\boldsymbol{\alpha}} = 0 \\
\implies &\boldsymbol{\xi_2} = -\omega_\xi^{-1} \omega_\alpha \dot{\boldsymbol{\alpha}} \\
\implies &\boldsymbol{\xi_2} = -A(\boldsymbol{\alpha})\dot{\boldsymbol{\alpha}} = -\begin{bmatrix} A_1(\boldsymbol{\alpha}), A_2(\boldsymbol{\alpha}) \end{bmatrix} \begin{bmatrix} \dot{\alpha}_1 \\ \dot{\alpha}_2 \end{bmatrix}
\end{aligned} \tag{3.10}$$

where $A(\boldsymbol{\alpha}) \in \mathbb{R}^{6\times 2}$ is known as the local form of a connection. It maps shape velocities to body velocities: $A(\boldsymbol{\alpha}) : T_{\alpha_1}S^1 \times T_{\alpha_2}S^1 \longrightarrow \mathfrak{se}(3)$. Eq. 3.10 is known as the *Kinematic Reconstruction Equation.*

3.3 Test for Controllability

Given the kinematic reconstruction equation, we are interested in determining a sequence of internal shape changes which steer the swimmer between two arbitrary poses *i.e.*, position and

orientation. We interpret the kinematic reconstruction equation, Eq. 3.10 as a nonlinear control system and use a controllability test to determine whether the system is controllable. Consider a non-linear control system with two inputs:

$$\begin{aligned} &\dot{\boldsymbol{x}} = f(\boldsymbol{x}, \boldsymbol{u}) = u_1 g_1 + u_2 g_2 \\ &\boldsymbol{x} \in \mathbb{R}^n \\ &f : \mathbb{R}^n \times \mathcal{U} \longrightarrow T_x\mathbb{R}^n \\ &g_1, g_2 : \mathbb{R}^n \longrightarrow T_x\mathbb{R}^n \\ &u_1, u_2 : [0, T] \longrightarrow \mathbb{R} \end{aligned} \tag{3.11}$$

Definition 1 *[34] The nonlinear control system defined by Eq.* (3.11) *is* ***controllable*** *if for any* $\boldsymbol{x_1}, \boldsymbol{x_2} \in \mathbb{R}^n$*, there exist control inputs* $u_1 : [0, T] \longrightarrow \mathbb{R}$ *and* $u_2 : [0, T] \longrightarrow \mathbb{R}$*, such that* $\boldsymbol{x}(0) = \boldsymbol{x_1}$ *and* $\boldsymbol{x}(T) = \boldsymbol{x_2}$ *where* $\boldsymbol{x}(t)$ *is the solution to the differential equation defined by Eq.* (3.11)*.*

Definition 2 *[34] The* ***accessibility Lie algebra*** $\mathcal{C}$ *for the system defined in Eq.* (3.11) *consists of linear combinations of repeated Lie brackets of the form*

$$\begin{aligned} &[g_p, [g_q, [\ldots, [g_1, g_2] \ldots]]], \\ &\qquad p, q, \ldots = \{1, 2\}. \end{aligned} \tag{3.12}$$

Definition 3 *[34] The* ***accessibility distribution*** $C(x)$ *is the subspace of* $\mathbb{R}^n$*, generated by evaluating the vector fields in* $\mathcal{C}$ *at a given point* $x \in \mathbb{R}^n$*, where*

$$C(x) = span\{X(x) | X \in \mathcal{C}, x \in \mathbb{R}^n\}. \tag{3.13}$$

Theorem 1 *(Chow) The system defined by Eq.* (3.11)*, is locally controllable near a point* $x \in \mathbb{R}^n$*, if*

$$dim\ C(x) = n.$$

For the swimmer, we assume that the state is defined using the integral of the body velocity $\boldsymbol{x}(t) = \int_{t_0}^{t} \xi(\tau) d\tau$. The quantity $\boldsymbol{x}(t)$ refers to the raw odometry for the robot, *i.e.*, the forwards minus backwards motion in each direction of the body frame. It does not account for the displacement of the body frame relative to the world frame, which is what we are interested in controlling (*i.e.* $g(t)$).

Nevertheless, it is known that for very small amplitude gaits, the raw odometry is approximately equal to the displacement of the swimmer in the world frame [22]. Hence, given a desired value of position and orientation of the swimmer's body frame relative to the world frame $g_{des}(T)$, we can seek small amplitude gaits, which result in $\boldsymbol{x}(T) \approx g_{des}(T)$. Further, if the swimmer's kinematic model *i.e.* Eq.3.10 is controllable, then there exist control inputs $u_1(t) = \dot{\alpha_1}$ and $u_2(t) = \dot{\alpha_2}$ which can result in this desired value of raw odometry. By scaling the duration and amplitude of these controls, we can ensure that the resulting gaits have small amplitude, which will ensure that the swimmer's raw odometry (and hence its displacement in the inertial frame) is equal to the displacement we desire. Hence, directly performing the

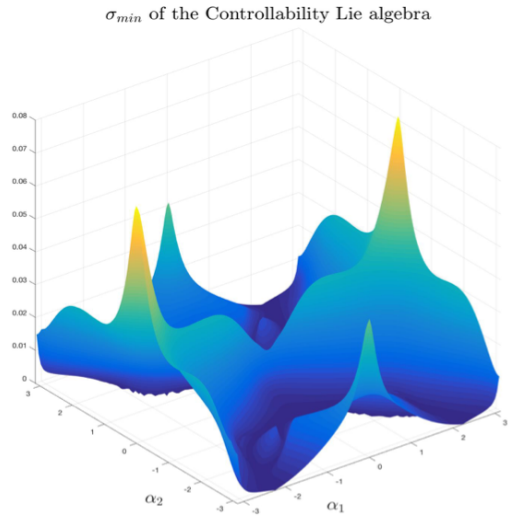

Figure 3.2: Minimum singular value of the controllability Lie algebra

test on Eq. 3.10 gives us a guarantee about the existence of control inputs for controlling the position and orientation of the swimmer in the inertial frame.

We perform this test as follows: from Eq. 3.11 and Eq. 3.10 , note that vector fields g_1 and g_2 can be chosen to be $-A_1(\boldsymbol{\alpha})$ and $-A_2(\boldsymbol{\alpha})$ respectively, where $A_1(\boldsymbol{\alpha})$ and $A_2(\boldsymbol{\alpha})$ are respectively the first and second column of the local connection $A(\boldsymbol{\alpha})$ from Eq. 3.10. Since $n = 6$, we need at least 6 vector fields to perform the controllability test. These vector fields are computed by taking Lie brackets of g_1 and g_2 as shown here:

$$\begin{aligned} g_1, g_2 &= -A_1(\boldsymbol{\alpha}), -A_2(\boldsymbol{\alpha}) \\ g_3 &= [g_1, g_2] \\ g_4, g_5 &= [g_1, g_3], [g_2, g_3] \\ g_6 &= [g_1, g_5] \end{aligned} \tag{3.14}$$

and we define

$$C(\boldsymbol{\alpha}) = span\{g_1(\boldsymbol{\alpha}), g_2(\boldsymbol{\alpha}), g_3(\boldsymbol{\alpha}), g_4(\boldsymbol{\alpha}), g_5(\boldsymbol{\alpha}), g_6(\boldsymbol{\alpha}) | \boldsymbol{\alpha} \in \mathcal{D}\}. \tag{3.15}$$

Note that these vector fields only depend on the shape angles α_1 and α_2. This allows us to numerically find the minimum singular value (σ_{min}) of the accessibility distribution over a domain $\mathcal{D} = D_1 \times D_2 \subset S^1 \times S^1$ where $D_1 = (0, 2\pi)$ and $D_2 = (-\pi, \pi)$ such that $\alpha_1 \in D_1$ and $\alpha_2 \in D_2$. The ranges for D_1 and D_2 are chosen to ensure that the links of the swimmer do not intersect each other. The minimum singular value gives a measure of linear independence amongst a set of vectors; if the minimum singular value of a square matrix C is greater than zero, then C is full rank and dim $C(\boldsymbol{\alpha}) = n$. By numerically evaluating $C(\boldsymbol{\alpha})$ over $\mathcal{D}$, we find that $\sigma_{min}(C(\boldsymbol{\alpha})) > 0$ for $\forall \boldsymbol{\alpha} \in \mathcal{D}$. This empirical calculation demonstrates that it is theoretically possible to determine controls $u_1(t)$ and $u_2(t)$ to steer the swimmer from an initial body frame odometry $\boldsymbol{x}(0) = \boldsymbol{x_1}$ to a final body frame odometry $\boldsymbol{x}(T) = \boldsymbol{x_2}$. In the next section, we demonstrate how we can use connection curvature functions to synthesize gaits, or a sequence of internal shape changes, for the swimmer.

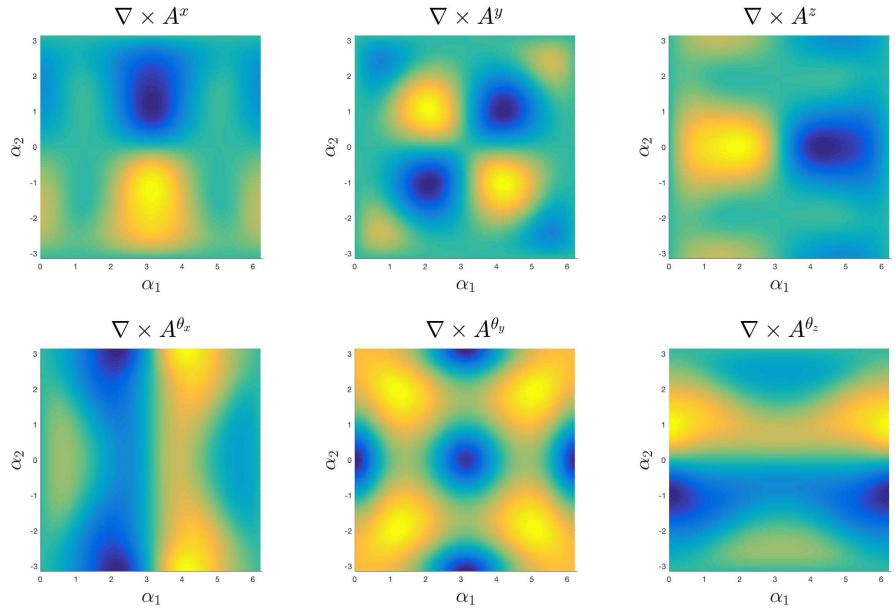

Figure 3.3: Connection Curvature Functions for the 3D swimmer computed using Eq. 3.18

3.4 Designing motion primitives

In the literature on geometric theory of swimming, the kinematic models in the form of Eq.3.10 have been successfully utilized to design gaits for the planar swimmer in low and high *Re* number regimes. According to [21, 24], Eq. 3.10 can be integrated over a gait γ (a closed loop in the shape space $\mathcal{D} \subset S^1 \times S^1$), to obtain the swimmer's raw odometry, *i.e.*, its net displacement along the body frame directions. Interpreting each row of $A(\boldsymbol{\alpha})$ as a vector field and the gait γ as defining an area on each of these fields, the line integral in Eq. 3.16 can be simplified by converting it into a surface integral Eq. 3.18 using the generalized Stokes theorem:

$$\int \boldsymbol{\xi} dt = -\int A(\boldsymbol{\alpha}(t))\dot{\boldsymbol{\alpha}}(t)dt \tag{3.16}$$

$$= -\int_{\gamma} A(\boldsymbol{\alpha})d\boldsymbol{\alpha} \tag{3.17}$$

$$= -\iint_{\mathcal{S}} \text{curl } A(\boldsymbol{\alpha})\ d\alpha_1 d\alpha_2. \tag{3.18}$$

Here, the integrand in Eq. 3.18 is the *curvature of the local connection* while $\mathcal{S}$ is the signed area enclosed by γ. We have converted the problem of finding line integrals of the rows of the local connection along gaits γ in Eq. (3.16) to calculating a surface integral of scalar curvature functions over $\mathcal{S}$ in Eq. (3.18). Since our shape space is two dimensional, we can visualize the connection curvature functions as surfaces over this two dimensional plane. This allows us to visually determine regions which enclose a net positive, negative or zero volume. The net volume enclosed by the curvature function over the area enclosed by the gait, is a direct measure of the displacement of the swimmer in that component on the body frame, as illustrated in Eq. (3.18). Fig. 3.3 shows the $(x, y, z, \theta_x, \theta_y, \theta_z)$ components of the *connection curvature functions* plotted as 2D surfaces over $\mathcal{D}$ where the surface height corresponds to the magnitude of curl $A(\boldsymbol{\alpha})$. We can use these surfaces as a visual tool for gait design by suitably parameterizing α_1 and α_2 to achieve a desired motion in the body frame.

Note that we are interested in steering the swimmer to a desired position and orientation in the world. For that, we would like to determine regions of the shape space which result in

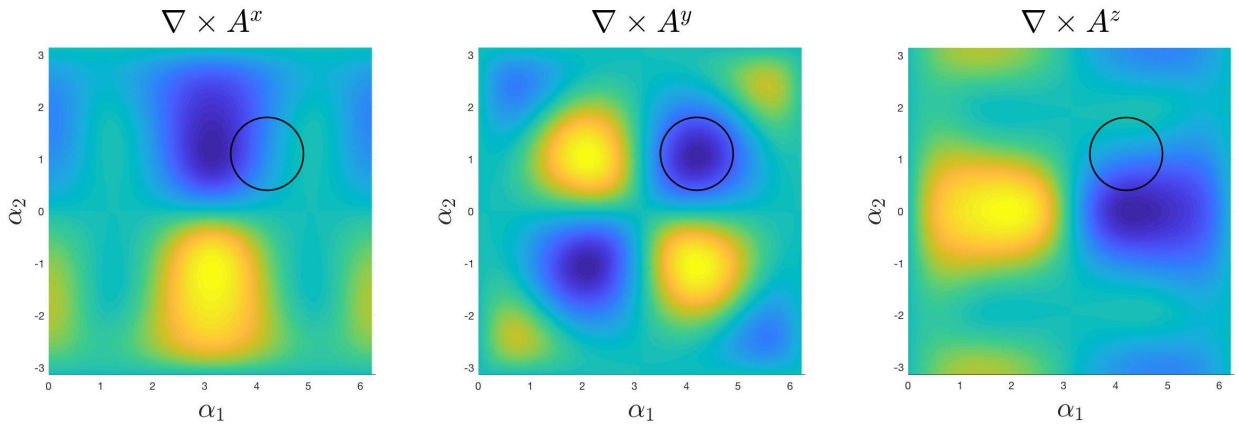

Figure 3.4: Translation gait overlaid on connection curvature functions.

a desired displacement of the swimmer relative to the world frame *i.e.* $g(T)$. On the other hand, the curvature function technique only gives us the ability to select gaits that results in displacement along a given body frame direction *i.e.* $x(T) = \int_{t_0}^{T} \xi(\tau) d\tau$. These two physical quantities are in general not equal, except for very small amplitude gaits in systems where the action of the Lie group can approximated to be Abelian [33]. Nevertheless, we know that these small amplitude gaits are inefficient as they expend a lot of energy in high frequency oscillations and produce small displacements per cycle, so it is desirable to consider large amplitude gaits for motion planning. We adopt this latter approach and explain how large amplitude gaits can be used make the swimmer translate along a fixed direction the world.

3.4.1 Translational Gaits

Designing gaits using the connection curvature functions poses a technical challenge as explained before. Thus, if we pick a circular gait as shown in Fig. 3.4 and parametrized in Eq. (3.19),(3.20),

$$\alpha_1(t) = 0.7 \sin(2\pi t) + 4.2 \tag{3.19}$$
$$\alpha_2(t) = 0.7 \cos(2\pi t) + 1.1 \tag{3.20}$$

hoping to get displacement predominantly along the Y_W axis of the world frame (which will serve as a Y_W motion primitive), we do end up getting displacement along other axes as well as shown in Fig. 3.5. Nevertheless, executing this gait for $T = 200$ cycles results in a displacement of approximately 13 body lengths along $\hat{\boldsymbol{d}} = [-0.5, 0.6, -0.62]$ where this displacement is calculated as follows (3.21):

$$d(T) = \frac{\|\boldsymbol{p}(T) - \boldsymbol{p}(0)\|_2}{L} \tag{3.21}$$

where $\boldsymbol{p}(t) \in \mathbb{R}^3$ is the position of the origin of the body frame attached to link 2 at time t and L is the length of the link. Note in the figure that the overall heading of the swimmer is along predominantly along $\hat{\boldsymbol{d}} = [-0.498, 0.599, -0.622]$. In the next section, we demonstrate a technique to adjust the initial orientation of the swimmer such that the overall heading during translation is predominantly along a desired direction.

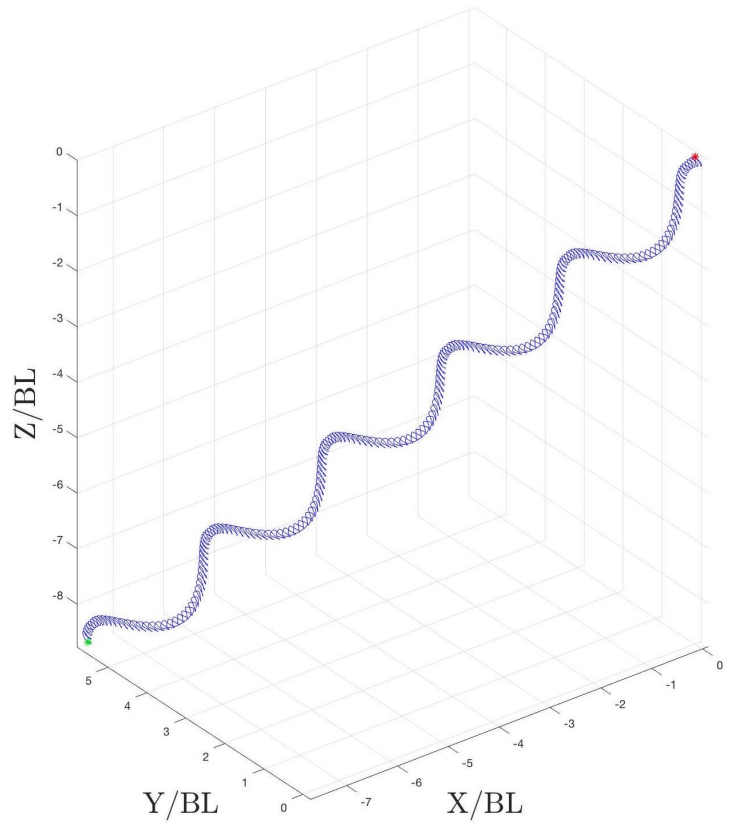

Figure 3.5: Trajectory resulting from executing $N = 200$ cycles of the gait in Eq. (3.19), (3.20).

3.4.2 Compensation for heading error

As we saw in Fig. 3.5, execution of the translation gait Eq. (3.19),(3.20) does not result in predominant motion along the Y_W axis as was desired, and instead makes the swimmer move along $\hat{\boldsymbol{d}} = [-0.5, 0.6, -0.62]$. To compensate for this difference, we propose to reorient the swimmer at $t = 0s$, in such a way that the new orientation, when followed by the same gait, makes the swimmer move along the desired direction. This can be interpreted as a point and shoot method where the first step of pointing corresponds to turning in place (reorienting) and the second step of shooting corresponds to executing the translational gait. We first describe how to compute the orientation into which the swimmer should be steered which will result in a desired direction of movement during translation. Following this, we synthesize gaits which can make the swimmer orient itself into that desired orientation R_{des}.

3.4.3 Averaged Body Frame

Starting from an orientation where the body frame of the swimmer is completely aligned with the world frame, we run the translational gait (Eq. 3.19,3.20) for $N = 100$ cycles and collect the trajectory data, $\boldsymbol{p_i} \in \mathbb{R}^3$ for $i = \{1, 2, ..., M\}$ corresponding to the position of the origin of the body fixed frame, where $M = N \times f$ where $dt = \frac{1}{f} = 0.01s$ is the sampling rate. Using singular value decomposition, we can extract the principal components of motion in the swimmer's

trajectory as follows:

$$P = \begin{bmatrix} \boldsymbol{p_1} \\ \boldsymbol{p_2} \\ \vdots \\ \boldsymbol{p_M} \end{bmatrix} \in \mathbb{R}^{M\times 3}$$
$$\text{svd}(P) = [U, S, V] \tag{3.22}$$

In this decomposition, U and V are orthogonal matrices whose columns are the left and right singular vectors of P. The columns of V form an orthonormal basis for $\mathbb{R}^3$. Hence, V can be interpreted as a rotation matrix that gives the principal components in the directions of the motion of the body frame through the duration of the trajectory. The first column of V gives the direction of maximum displacement. Now, if we want the average motion of the swimmer to be along X_W axis of the world frame, we use $R_{des} = V^{-1} = V^*$ as the initial body frame orientation. In order to steer the swimmer to this orientation, we execute a sequence of rotation gaits as described below.

3.4.4 Gaits for rotations

From the connection curvature functions corresponding to rotation about the body frame's x, y, z axes, we can synthesize gaits which achieve a desired rotation about those axes. The gait for rotation about x_b axis of the body frame can be chosen to be:

$$\begin{aligned} \alpha_1(t) &= -0.707\sin(2\pi t) + \pi \\ \alpha_2(t) &= -0.707\sin(4\pi t) \end{aligned} \tag{3.23}$$

The gait for rotation about y_b axis of the body frame is:

$$\begin{aligned} \alpha_1(t) &= 0.3\sin(2\pi t) + \pi \\ \alpha_2(t) &= 0.3\cos(2\pi t) \end{aligned} \tag{3.24}$$

The gait for rotation about z_b axis of the body frame is:

$$\begin{aligned} \alpha_1(t) &= -0.707\sin(4\pi t) + \pi \\ \alpha_2(t) &= 0.707\sin(2\pi t) \end{aligned} \tag{3.25}$$

The plots in Figs. 3.6, 3.7, 3.8 show that each rotation gait is decoupled from other gaits. For example, executing the gait for rotation about the longitudinal axis *i.e.* Eq. 3.24 does not result in rotation about the lateral axes. This is because the total area enclosed in the circle in the curvature functions for x_b and z_b is zero. Similarly, executing the gait for rotation about x_b axis *i.e.* Eq.3.23 does not result in rotation about the y_b and z_b axes. Hence these gaits are decouple from one another. We can execute these gaits sequentially in order to to steer the swimmer to any orientation. To steer the swimmer into the desired orientation *i.e.* R_{des}, we refer the reader to approach outlined in Algorithm ~ 1.

Using V^{-1} as an initial orientation, we are able to get translation of the swimmer along X_W axis of the world frame as shown in Fig. 3.9. Following a similar approach, we can determine the initial orientation which will result in dominant motion along other direction in the world frame. Finally, starting from those orientations, we can execute the translation gait that will make the swimmer move along those directions.

Algorithm 1 Algorithm for turning in place

1: Execute the gait for rotation about x_b axis for one cycle starting from the identity orientation and record its geometric phase *i.e.* total rotation increment about the x_b axis through this cycle: G_{θ_x}. Repeat this for other rotation gaits and record their phases as $G_{\theta_y}, G_{\theta_z}$
2: Convert the desired orientation R_{des} to body frame angles α, β, γ which correspond to rotation about x_b, y_b, z_b axes
3: Determine number of cycles for each gait using $N_{\theta_x} = \alpha/G_{\theta_x}, N_{\theta_y} = \beta/G_{\theta_y}, N_{\theta_z} = \gamma/G_{\theta_z}$
4: Execute Rot_{x_b} gait for N_{θ_x} cycles, followed by Rot_{y_b} gait for N_{θ_y} cycles and Rot_{z_b} gait for N_{θ_z} cycles

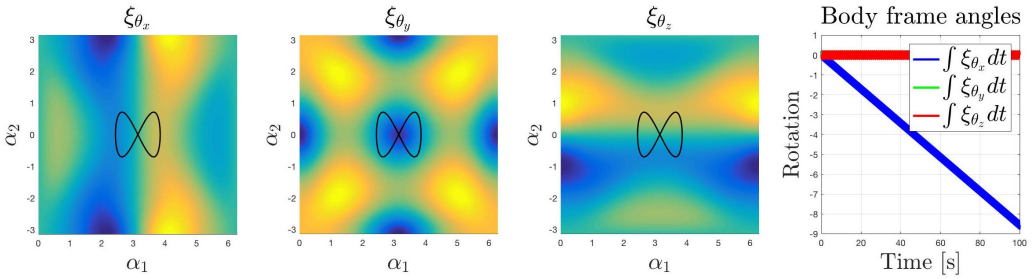

Figure 3.6: Gait for rotation about x_b

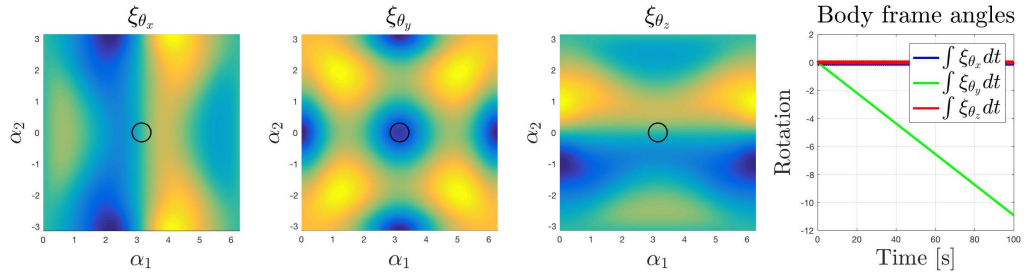

Figure 3.7: Gait for rotation about y_b

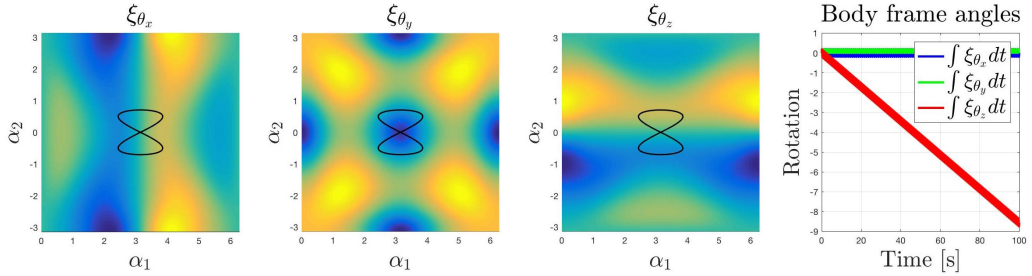

Figure 3.8: Gait for rotation about z_b

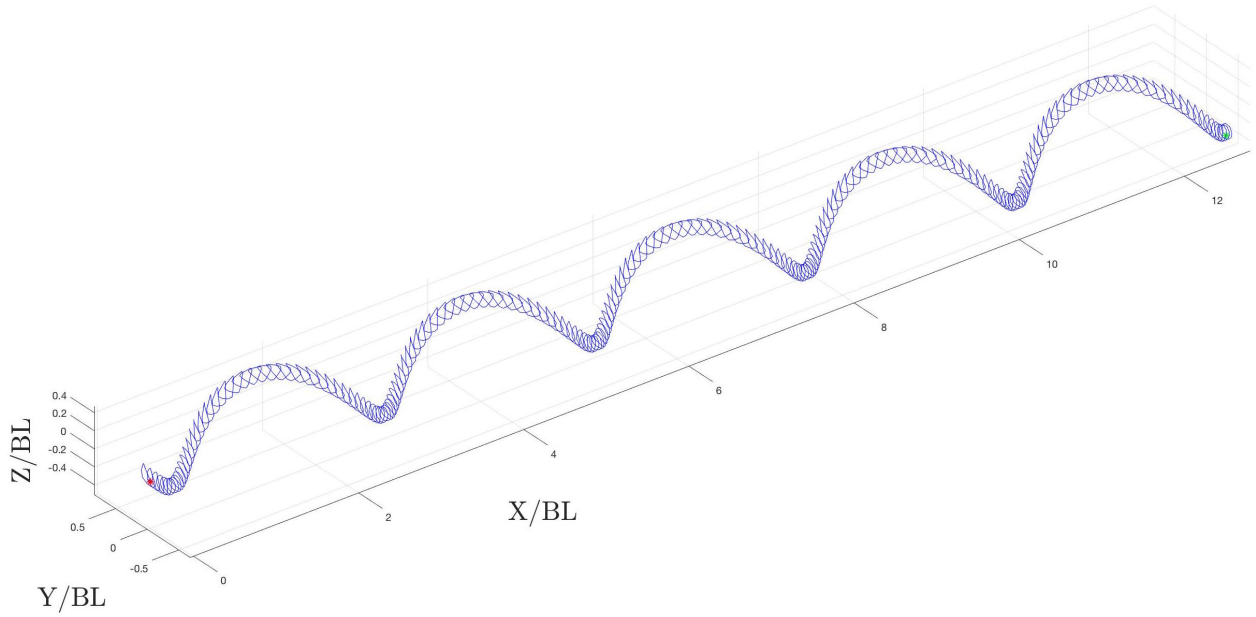

Figure 3.9: Trajectory resulting from executing the gait in Eq. (3.19),(3.20) with initial orientation V^{-1}

3.5 Experimental Validation

We devised a 3D swimming robot shown in Fig. 3.10 as a testbed for our simulations. This robot consists of two Longrunner metal gear microservos that are controlled by direct PWM using an ESP8266 microcontroller with an integrated WiFi module. A mobile application communicates directly with the onboard controller that allows different gaits to be programmed on the swimmer. Using this application, we can also update gait parameters such as offsets, frequencies, cycles and amplitudes for each of the two servos. Each link of the swimmer has a length of 7 cms. The first and third links are paddles whereas the second link contains all the electronics, so it is comparatively bulkier. The swimmer was submerged in a tank of corn syrup which has a viscosity in the range of 50-100 cps and density close to 1.37 g/ml. Several gaits

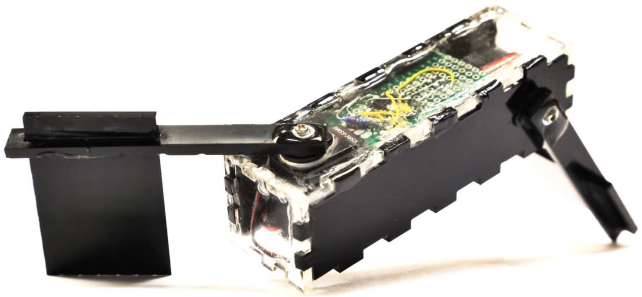

Figure 3.10: 3D Swimmer Robot

were implemented on the 3D swimmer to demonstrate the validity of the trajectories derived in simulations. For the sake of brevity, only results for a translation gait along the length of the tank and rotation about y_b axis of the body frame are shown here.

In the translation gait [1], the frequency at which the links rotate results in an average

[1] `https://youtu.be/BcT5ps1mTFE`

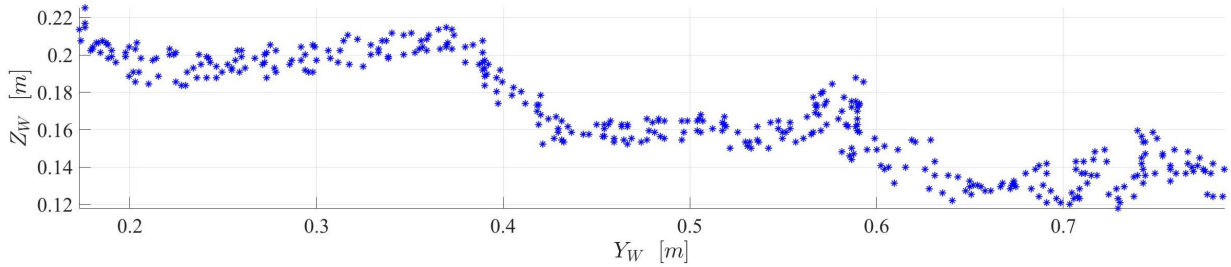

Figure 3.11: Trajectory of the 3D Swimmer executing the translational gait (Side View)

translational velocity close to 0.0017 m/s (determined from experiments). Using these parameters, the resulting Re number $Re \approx 1.5 < 100$. Hence swimming at this regime with these parameters is largely dominated by low-Re number hydrodynamics. To ensure that the swimmer has dominant motion along the longer side of the tank (Y_W), we experimented with the initial orientation of the swimmer and through several trials empirically determined an approximate orientation that would make it swim along the longer side of the tank. Fig. 3.11 shows the trajectory of the center of mass of the 3D swimmer as it executes the translation gait. These points were hand tracked using *Tracker: Video Analysis and Modeling Tool*. Notice in Fig. 3.11 that the swimmer has maximal displacement along the longer length of the tank (Y_W) $\sim$ 65 cms, however, it also has nonzero displacement along the other sides as well, which are $\sim$10 cms along the depth (Z_W) and $\sim$15 cms along the width (X_W) of the tank. This extraneous displacement can be attributed to two reasons: First, the swimmer is not perfectly neutrally buoyant. This could be the result of unwanted air bubbles in the swimmer. These bubbles cannot easily escape the swimmer's body because of the viscosity of the corn syrup. As a result, the swimmer is not perfectly neutrally buoyant like it was assumed in the model. The swimmer's body experiences a torque about the lateral axes due to the force of buoyancy and this torque warps the orientation the swimmer. Moreover, this deviation keeps changing throughout the duration of the experiment as the swimmer's body rotates. Due to this, when the swimmer executes the translation gait, we observe displacement along the lateral side of the tank as well. However, as we can see in Fig. 3.11, the dominant displacement is still along the length of the tank as was expected.

In Fig. 3.12, we show a qualitative comparison of the robot's trajectory with the trajectory derived from the simulation. The simulated trajectory has been rotated and superimposed on the robot's trajectory for a better comparison. The values of the physical dimensions of the model in the simulation were kept the same as those of the actual robot. The duration of simulation was $T = 236s$ which was roughly the number of cycles for which the swimmer's paddles oscillated. The only difference between the simulation and experiment was the angular speed of the joint angles. We notice in the figure that the observed trajectory behaves qualitatively similar to the trajectory calculated from simulations. However, we do not observe full circles in the helix of the robot's trajectory, which can be attributed to the non-slender shape of the robot's links.

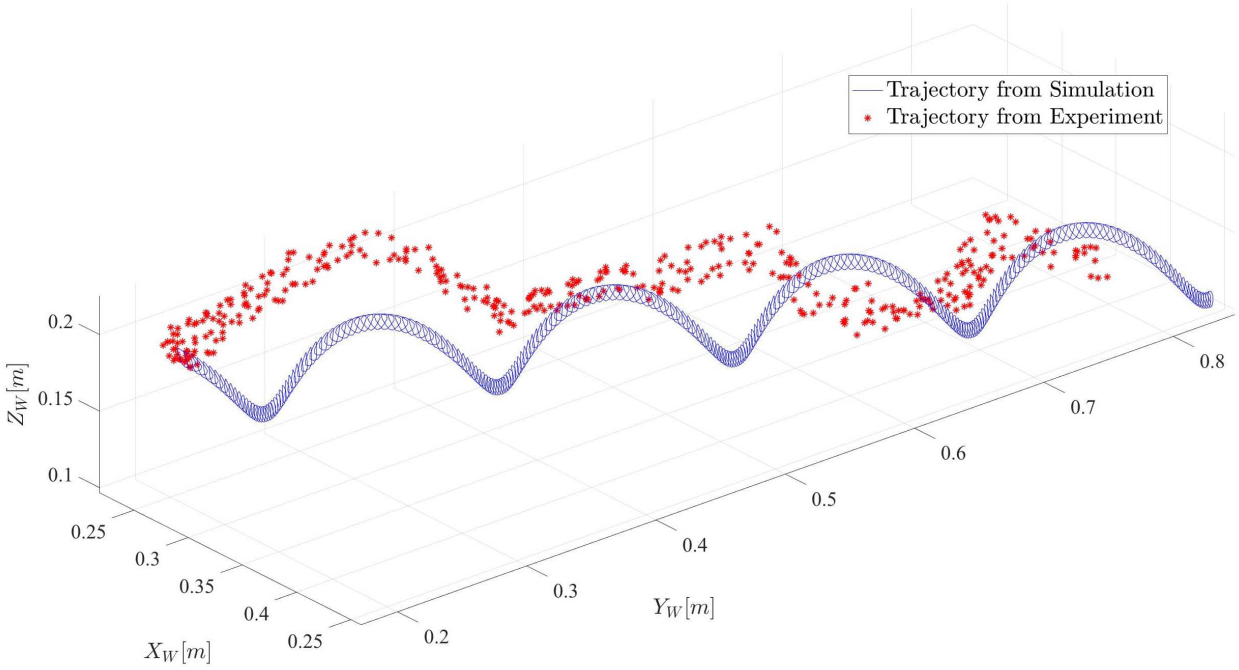

Figure 3.12: Translation gait comparison

In the next experiment we implement the rotation gait on the robot. The swimmer was placed in the tank with its body frame aligned with the world frame. Following this, the gait corresponding to rotation about the longitudinal axis of the body frame y_b was implemented. This gait is depicted in Fig. 4b and described in Eq. 3.24. The corresponding video can be found in the link at the footnote [2]. Fig. 3.14 shows snapshots of the side view and top view of the robot. This gait rotates the swimmer about its longitudinal axis with negligible rotation about other axes, which is also in agreement with simulated results.

[2] `https://youtu.be/2o0w4attCmE`

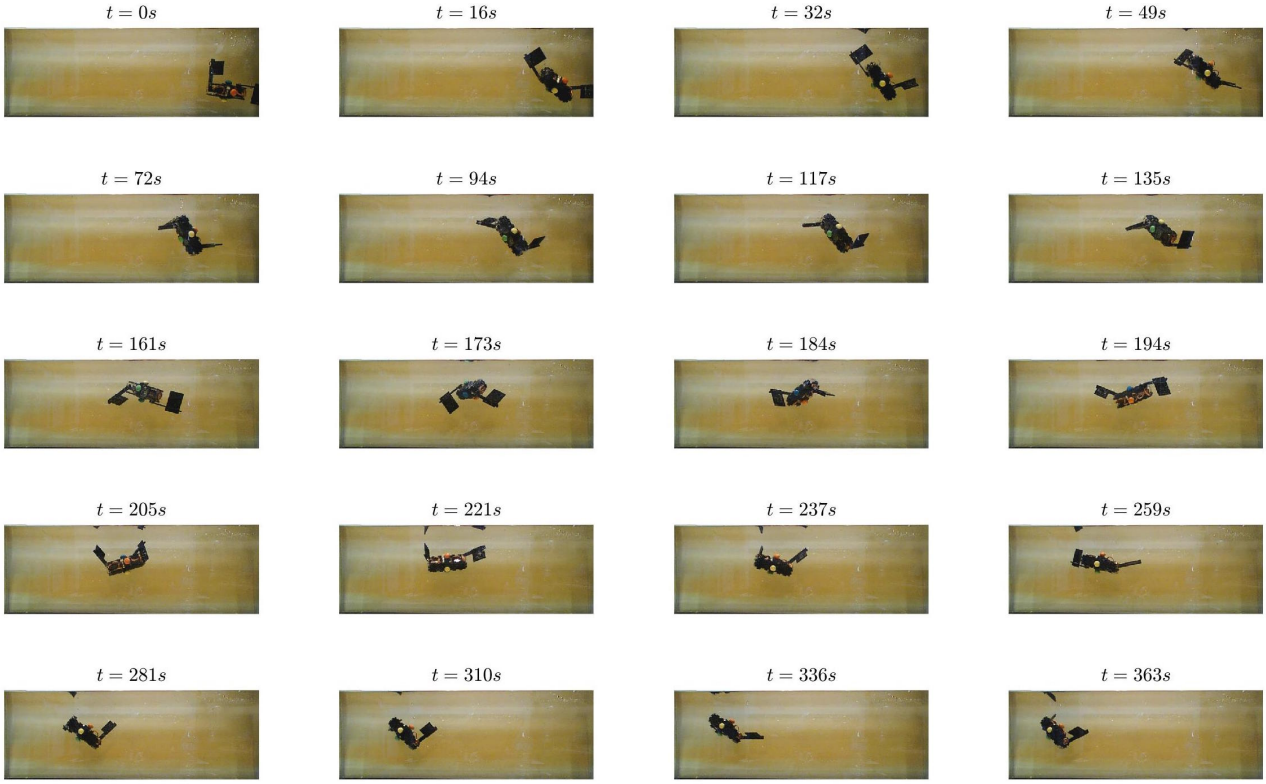

Figure 3.13: Snapshots of the side view of the 3D Swimmer executing the translation gait

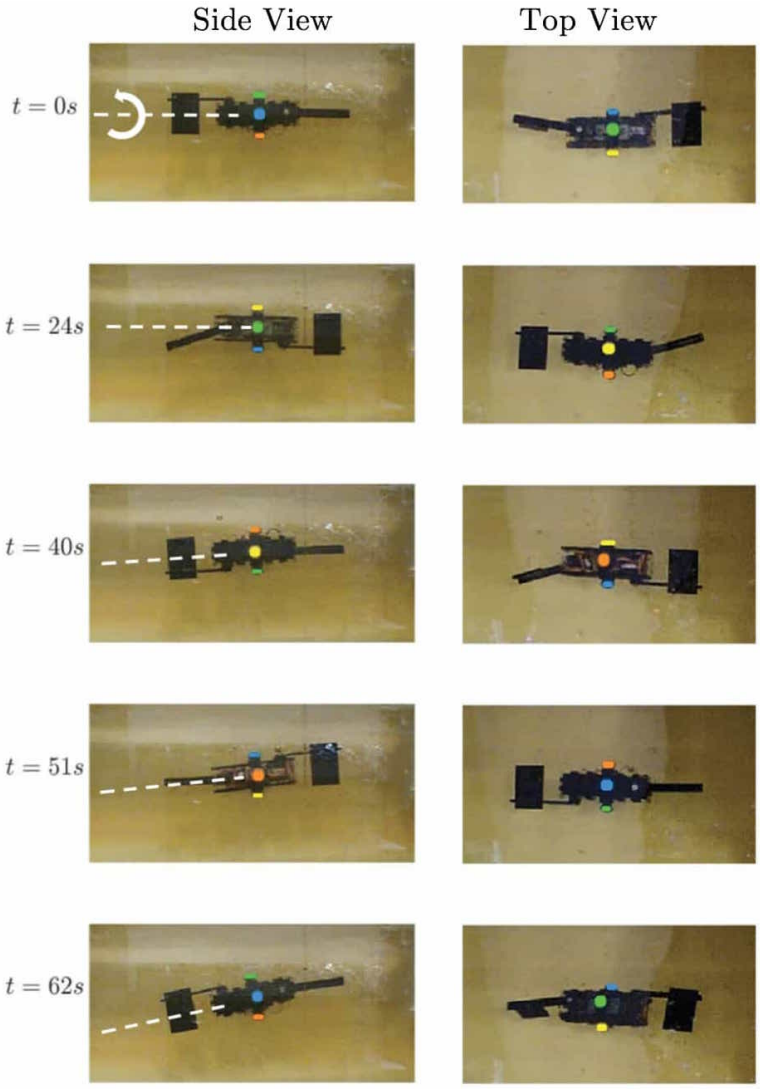

Figure 3.14: Snapshots of the top view and side view of the 3D Swimmer executing the gait that results in rotation about its longitudinal axis

3.6 Conclusions

In this chapter, we have considered the problem of synthesizing motion primitives for a three dimensional version of Purcell's planar swimmer. Using the notion of connection curvature functions, we have designed gaits for the 3D swimmer which result in translation and rotation of the swimmer's body frame. These custom gaits have also been implemented on a robot and we have demonstrated that with a suitable choice of initial orientation, we can make the swimmer move along a desired direction in the world frame in simulation. From the experiments, we observed errors in the heading of the swimmer which were attributed to imperfect assumption of neutral buoyancy and the torque acting on the swimmer's body due to the force of buoyancy. Additionally, the links of the robot are not perfectly slender as is required in RFT. As a part of future work, we propose to model the effects of non-slenderness and buoyancy in the swimmer's motion, and accommodate their effects in the gait design approach. Furthermore, we are also interested in extending the gait design technique to a multiple link version of the 3D swimmer by interpreting this as a discretization of a continuum snake. We hypothesize that this redundancy in design will allow the swimmer to execute dexterous maneuvers which could be useful for navigating in a constrained environment.

Chapter 4

Motion planning for an externally actuated swimmer

4.1 Introduction

In the last chapter, we described a swimmer capable of locomoting in a three dimensional low-Re number regime. This swimmer was internally actuated using servos at the two joints which allow for direct control over its internal shape. However, in such a regime, the minimum joint torque that is required to produce a desired angular velocity imposes a constraint on the capacity of the motors. This restriction on the minimum size of the motors and ultimately the size of the robot prevents scaling these swimmers to micrometer dimensions. Additionally, the overall system integration with sensors, computation and actuation at the microscale becomes even more challenging [38]. Finally, the susceptibility of internally actuated robots to electrical/mechanical failure prohibits the application of such systems for in-situ operations. These limitations point towards the need to develop a system with minimal complexity whilst still retaining the basic locomotive functionalities at the micrometer scale. Towards that end, actuation using external time-varying magnetic fields has been proposed as a feasible approach to generate propulsion in robots at the microscopic scale [8, 36]. In this chapter, we will explore mathematical models of articulate discrete swimmers consisting of magnetic links connected via rotary joints / springs and dwell on how to synthesize motion primitives for these swimmers. We conclude this chapter with experimental results and directions for future work.

4.1.1 Contributions

In this chapter, we consider a two link and three link magnetic swimmer similar to the ones proposed in [1, 18, 19, 3]. The links in these swimmers are assumed to be ferromagnetic and connected to each other with flexible rotary joints.

1. Building on these works, we demonstrate how a richer class of magnetic fields can be generated to induce net locomotion in these swimmers by exploiting structural properties in the system dynamics. We describe how tools similar to curvature functions can be used to motivate the control inputs proposed in previous works and how new control inputs can be computed using these tools without having to use numerical trajectory optimization algorithms which are susceptible to local minima.

2. We perform a systematic design optimization of a three-link swimmer to determine the numerical values of internal magnetizations for optimizing swimmer performance. We

describe a principled approach on how to encode these precise magnetization patterns in millimeter scale magnetoelastic swimmers and demonstrate locomotion and turn-in-place maneuvers in a viscous regime using two pairs of Helmholtz coils.

4.1.2 Outline

In Section 4.2, we present the mathematical model of a two link and three link magnetoelastic swimmer based on the derivations in Chapter 2. In Section 4.3, we describe the trajectories of two and three link swimmer resulting from crossed uniform and transverse oscillating fields and dwell on how to modify these control inputs to generate a turning in place motion for the two link swimmer. Using tools from perturbation theory, we perform a numerical optimization to compute the optimum magnetization constants for a three link swimmer which maximize is forward displacement per cycle. In Section 4.5, we demonstrate how to motivate previously proposed control inputs using a geometric argument and describe how novel control inputs can be synthesized. In Section 4.6 we describe our approach to fabricate millimeter scale swimmers and a principled method of encoding the optimal magnetization constants in these swimmers. We describe the setup and experimentally verify the trajectories from simulations on these swimmers using Helmholtz coils.

4.2 Mathematical Model

We will focus on a planar model of a two link and three link swimmer. We refer the reader to the derivations introduced in Section 2.1 and 2.2 in Chapter 2. A brief review of notation is presented here.

Figures 4.1a and 4.1b shows the top view of a two and three link swimmer which is made up slender uniformly magnetized links. In each of the swimmers, the longitudinal axis of the body frame is denoted by $\hat{\boldsymbol{t}}$ and the lateral axis of the body frame is denoted by $\hat{\boldsymbol{n}}$. In the given representation, it is easy to see that $\hat{\boldsymbol{t}} = (\cos\theta, \sin\theta)$ and $\hat{\boldsymbol{n}} = (-\sin\theta, \cos\theta)$ where θ is the angle between $\hat{\boldsymbol{t}}$ and X_w. The swimmers are submerged in a liquid of uniform viscosity and the associated drag coefficients are c_t, c_n. The entire plane is under the influence of a spatially uniform magnetic field $\boldsymbol{B}(t) = (B_x(t), B_y(t))$ where B_x denotes the horizontal (along X_W) component of the spatial magnetic field $\boldsymbol{B}(t)$ and likewise B_y denotes the vertical (along Y_W) component of the spatial magnetic field.

Elastic Effects

In the derivations introduced in Section 2.1 and 2.2 in Chapter 2, we did not account for elastic effects at the spring joint between the links. We now consider the effects of adding a flexible joint between two links. This can be modeled by assuming that each consecutive pair of links is connected to each other via flexible torsional springs. In an articulate swimmer which is made using a continuum filament, the value of the spring stiffness is determined using the modulus of elasticity, the second moment of area and length of the filament. The spring at joint serves to provide a restoring torque on both links in accordance with Hooke's law:

$$\boldsymbol{\tau}_{spring} = -\kappa(\theta_{l+1} - \theta_l) \tag{4.1}$$

where l is the index of the link.

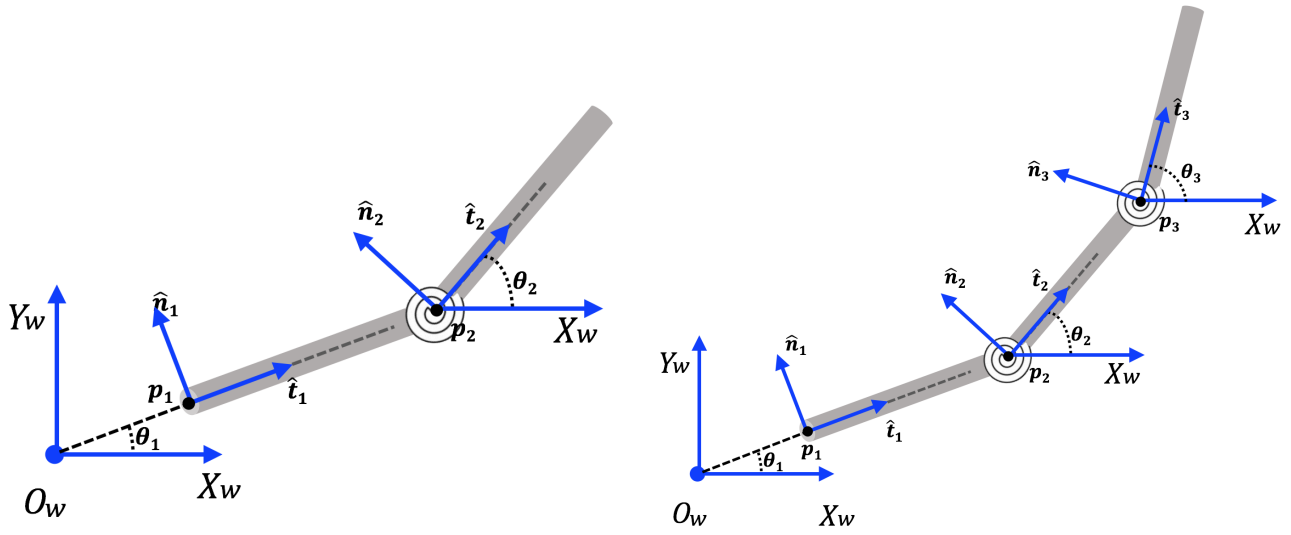

(a) Top view of a two link magneto elastic swimmer (b) Top view of a three link magneto elastic swimmer

Figure 4.1: Schematic of Two and Three link magnetic swimmers

4.2.1 Complete Model

We now present the complete model of a two link and a three link magnetic swimmer, by incorporating hydrodynamic, elastic and magnetic effects.

Two-Link Swimmer

Consider a two link swimmer as shown in Figure 4.1a. The configuration space of this swimmer is $Q = SE(2) \times S^1$ where the first component $SE(2)$ corresponds to the position and orientation of the body fixed frame of the first link relative to the world. The second component corresponds to the orientation of the second link relative to the world. Hence the configuration variable is $\boldsymbol{q} = (x, y, \theta_1, \theta_2) = (\boldsymbol{p_1}, \theta_1, \theta_2)$. Let the corresponding velocity be denoted by $\dot{\boldsymbol{q}} = (\dot{\boldsymbol{p}}_1, \dot{\theta}_1, \dot{\theta}_2)$. The position and velocity of the body frame attached to link 2 can be expressed using

$$\begin{aligned}
\boldsymbol{p}_2(t) &= \boldsymbol{p}_1(t) + L\hat{\boldsymbol{t}}(t) \\
\dot{\boldsymbol{p}}_2(t) &= \dot{\boldsymbol{p}}_1(t) + L\dot{\theta}_1\hat{\boldsymbol{n}}(t) \\
\dot{\boldsymbol{p}}_3(t) &= \dot{\boldsymbol{p}}_3(t) + L\dot{\theta}_3\hat{\boldsymbol{n}}(t) \text{ (in three link)}
\end{aligned}$$

To analyze the complete dynamics, we describe all the sources of forces and torques acting on the two links. These are listed here:

1. Hydrodynamic Drag Forces
   (a) $\boldsymbol{F}_{1,h}$: Hydrodynamic drag force on link 1 expressed in the world frame
   (b) $\boldsymbol{F}_{2,h}$: Hydrodynamic drag force on link 2 expressed in the world frame
2. Hydrodynamic Drag Torques
   (a) $\boldsymbol{\tau}_{1,h}^{p_1}$: Hydrodynamic drag torque on link 1 relative to $\boldsymbol{p}_1$ expressed in the world frame
   (b) $\boldsymbol{\tau}_{2,h}^{p_1}$: Hydrodynamic drag torque on link 2 relative to $\boldsymbol{p}_1$ expressed in the world frame
   (c) $\boldsymbol{\tau}_{2,h}^{p_2}$: Hydrodynamic drag torque on link 2 relative to $\boldsymbol{p}_2$ expressed in the world frame

3. Magnetic Torques

   (a) $\boldsymbol{\tau}_{1,m}$: Magnetic torque on link 1 expressed in the world frame

   (b) $\boldsymbol{\tau}_{2,m}$: Magnetic torque on link 2 expressed in the world frame

4. Spring Torque

   (a) $\boldsymbol{\tau}_{2,spring}$: Torque due to the torsional on link 2.

From the assumptions of resistive force theory, the net force and moment on a system in a quasi-static equilibrium vanishes. This gives:

$$\boldsymbol{F}_{1,h} + \boldsymbol{F}_{2,h} = 0 \tag{4.2a}$$

$$\hat{\boldsymbol{e}}_z \cdot (\boldsymbol{\tau}_{1,h}^{\boldsymbol{p}_1} + \boldsymbol{\tau}_{2,h}^{\boldsymbol{p}_1} + \boldsymbol{\tau}_{1,m} + \boldsymbol{\tau}_{2,m}) = 0 \tag{4.2b}$$

$$\hat{\boldsymbol{e}}_z \cdot (\boldsymbol{\tau}_{2,h}^{\boldsymbol{p}_2} + \boldsymbol{\tau}_{2,m}) = \boldsymbol{\tau}_{2,spring} \tag{4.2c}$$

We can rewrite Eqs. 4.2a-4.2c in the form of a control affine system. The control input to the system is defined by the spatial magnetic fields *i.e.* $\boldsymbol{u} = (B_x(t), B_y(t))$ and the state of the system is precisely given by $q(t)$. The following system of equations demonstrates how the dynamics of the system is captured by first order nonlinear ODEs:

$$\begin{aligned} \dot{\boldsymbol{q}} &= \boldsymbol{f}(\boldsymbol{q}) + \boldsymbol{g}_1(\boldsymbol{q})B_x(t) + \boldsymbol{g}_2(\boldsymbol{q})B_y(t) \\ &= \boldsymbol{f}(\boldsymbol{q}) + \boldsymbol{G}(\boldsymbol{q})\boldsymbol{u} \\ \boldsymbol{q} &\in \mathbb{R}^4 \ (SE(2) \times S^1) \\ \boldsymbol{f} &: \mathbb{R}^4 \longrightarrow T_x\mathbb{R}^4 \\ B_x, B_y &: [0, T] \longrightarrow \mathbb{R} \end{aligned} \tag{4.3}$$

The drift component $\boldsymbol{f}(\boldsymbol{q})$ arises due to the restoring torque of the spring, whereas the driftless components $\boldsymbol{g}_1(\boldsymbol{q}), \boldsymbol{g}_2(\boldsymbol{q})$ are due to the drag forces and magnetic torques. If we make the assumption that the links are connected with pinned joints, we can eliminate the effects of compliance by setting $\kappa = 0$ in Eq. 4.3 above. The resulting dynamics are akin with driftless control affine systems as described in Eq. 4.4.

$$\begin{aligned} \dot{\boldsymbol{q}} &= \boldsymbol{g}_1(\boldsymbol{q})B_x(t) + \boldsymbol{g}_2(\boldsymbol{q})B_y(t) \\ &= \boldsymbol{G}(\boldsymbol{q})\boldsymbol{u} \end{aligned} \tag{4.4}$$

Three link swimmer

Following the derivation of the two link swimmer, we can write the force and torque balance equations for the three link swimmer as well.

$$\boldsymbol{F}_{1,h} + \boldsymbol{F}_{2,h} + \boldsymbol{F}_{3,h} = 0 \tag{4.5a}$$

$$\hat{\boldsymbol{e}}_z \cdot (\boldsymbol{\tau}_{1,h}^{\boldsymbol{p}_1} + \boldsymbol{\tau}_{2,h}^{\boldsymbol{p}_1} + \boldsymbol{\tau}_{3,h}^{\boldsymbol{p}_1} + \boldsymbol{\tau}_{1,m} + \boldsymbol{\tau}_{2,m} + \boldsymbol{\tau}_{3,m}) = 0 \tag{4.5b}$$

$$\hat{\boldsymbol{e}}_z \cdot (\boldsymbol{\tau}_{2,h}^{\boldsymbol{p}_2} + \boldsymbol{\tau}_{3,h}^{\boldsymbol{p}_2} + \boldsymbol{\tau}_{2,m} + \boldsymbol{\tau}_{3,m}) = \boldsymbol{\tau}_{2,spring} \tag{4.5c}$$

$$\hat{\boldsymbol{e}}_z \cdot (\boldsymbol{\tau}_{3,h}^{\boldsymbol{p}_3} + \boldsymbol{\tau}_{3,m}) = \boldsymbol{\tau}_{3,spring} \tag{4.5d}$$

Once again, we can rewrite Eq. 4.5a-4.5d in the form of a control affine system in the state variable $\boldsymbol{q}(t)$. The state variable $\boldsymbol{q}(t)$ in the case of a three link swimmer includes the additional orientation of the third link. Hence the total configuration space is $Q = SE(2) \times S^1 \times S^1$ *i.e.* $\boldsymbol{q} = (\boldsymbol{p}_1, \theta_1, \theta_2, \theta_3)$. The control inputs in this case would still be the spatial components of the magnetic field in the X_w, Y_w frame. The resulting equations of motion are similar to Eq. 4.3 above.

4.2.2 Making the equations of motion dimensionless

Table 4.1: Physical parameters relevant to the dynamics of the magneto-elastic swimmer

Parameter	**Symbol**	**Numerical value with units**
Spring constant	κ	0.01 [Nm]
Drag Coefficient	ξ	0.1 [Nsm^{-2}]
Magnetic field amplitude	B	1 [T]
Saturation magnetization	$\boldsymbol{M}$ or h	1 [Am^{-1}]
Internal magnetization parameters	(m_t, m_n)	$[-1, 1]$ [Unitless]
Characteristic Length	L	1 [m]

In order to reduce the dimension of the parameter space, we use a technique called normalization or non-dimensionalization. This procedure helps to reduce the number of physical parameters used to describe the dynamics in way that retains the original information in the dynamics. Instead of dealing with several physical parameters, the idea is to deal with ratios of these parameters by converting the governing differential equations into a unit-less form. This is not only suitable for numerical simulations, it also gives an intuitive insight on the behavior of the system as a function of few characteristic parameters. While the technique followed in [18] identifies the characteristic time scales based on breaking the full system into individual sub-systems, we arrive at identical scales based on investigating the full dynamics. There are three characteristic parameters that determine the dynamics of the system (1) the visco-magnetic time constant $T_m = \frac{\xi L^2}{BM}$ (2) the visco-elastic time constant $T_k = \frac{\xi L^3}{\kappa}$ and (3) the characteristic length L. From now onwards, we will assume that the equations of motion have been converted to a non-dimensional form (Eq. 4.7)

$$\dot{\bar{\boldsymbol{q}}} = \bar{\boldsymbol{f}}(\bar{\boldsymbol{q}}) + \bar{\boldsymbol{g}}_1(\bar{\boldsymbol{q}})\bar{B}_x(\bar{t}) + \bar{\boldsymbol{g}}_2(\bar{\boldsymbol{q}})\bar{B}_y(\bar{t}) \tag{4.6}$$

where

$$\bar{\boldsymbol{q}} = T\boldsymbol{q},\ \bar{t} = \frac{t}{T_m},\ \alpha = \frac{T_m}{T_k} \tag{4.7}$$

The transformation matrix T is defined as

$$T = \begin{bmatrix} \frac{1}{L} & 0 & 0 & 0 \\ 0 & \frac{1}{L} & 0 & 0 \\ 0 & 0 & 1 & 0 \\ 0 & 0 & 0 & 1 \end{bmatrix} \tag{4.8}$$

We will omit the overbar in the subsequent sections and assume the equations of motion are dimensionless implicitly.

4.3 Two Link Swimmer Simulations

In the previous sections, we formulated the equations of motion for a two and three link magnetoelastic swimmer. Based on those equations, we can explore the behavior of the swimmer's motion as a function of different types of control inputs. We first investigate the trajectories of the swimmer based on control inputs previously proposed in literature and in Section 4.5 describe how to design novel motion plans using geometric arguments. For simplicity, we will consider swimmers with tangential magnetization components only *i.e.* $m_n^i = 0 \; \forall i \in \{1, 2\}$ where index i corresponds to the link number. Authors in [18] demonstrated that the two link swimmer with tangential magnetizations can achieve net locomotion in crossed uniform and oscillating fields when either of the following conditions are met:

1. The tangential magnetizations in the two links are non-zero, mutually unequal $m_t^1 \neq m_t^2$ and the joint connecting the links is pinned with no spring *i.e.* $\kappa = 0$

2. The tangential magnetizations in the two links are mutually unequal $m_t^1 \neq m_t^2$ and the joint connecting the links has a torsional spring *i.e.* $\kappa \neq 0$

3. One of the links is non-magnetic *i.e.* $m_t^1 = 0, m_t^2 \neq 0$ and the joint connecting the links is equipped with a torsional spring *i.e.* $\kappa \neq 0$

In consonance with these conditions, we now provide simulation results corresponding to the case where $m_t^1 \neq m_t^2, \kappa = 0$ and for $m_t^1 = 0, m_t^2 \neq 0, \kappa \neq 0$. The physical parameters we use for these simulations are provided in Table 4.2.2.

4.3.1 Trajectories without elastic effects

For the case where the two link swimmer does not have a torsional spring at the joint, we will use Eq. 4.4 for numerical simulations. The drift component in these equations is zero because there is no spring. Hence, as soon as the external magnetic field is switched off, the configuration of the swimmer just before switching the field off, persists forever. In the following subsections, we will demonstrate how using different versions of crossed uniform and oscillating magnetic fields can result in net locomotion. We will assume that link two has a magnetization component that is twice as strong as the magnetization of link one *i.e.* $m_t^1 = 0.5, m_t^2 = 1$. Analytical proofs for why such asymmetry is necessary for locomotion are provided in [2].

Translation

Using $B_x(t) = 1, B_y(t) = \sin \omega t$ results in locomotion of the swimmer along X_w axis of the world frame. From now on, we will denote this primitive as $\boldsymbol{u}_{trans}$ *i.e.* $\boldsymbol{u}_{trans} = (1, \sin \omega t)$. For this simulation, we selected the actuating frequency using by numerically simulating the dynamics over a range of frequencies and selected the one that gives the maximum displacement per cycle. Results from [27] describe that for a given number of cycles of the external field, the displacement of the swimmer depends on the frequency of the field in a way that is akin to a resonance like behavior. The swimmer undergoes almost negligible displacement at very low and very high frequencies, while a peak value of displacement is obtained at some intermediary frequency. Through a sweep over a range of 0 to 100 Hz, we concluded that the swimmer translates by the maximum (over $T_{max} = 100s$) at $f \sim 8Hz$ ($\omega = 16\pi[rad/s]$) (see Figure 4.2). The exact value was 7.6Hz. The corresponding trajectory of the swimmer is shown in Figure. 4.4. The direction of motion of the swimmer is along the constant component of the external field

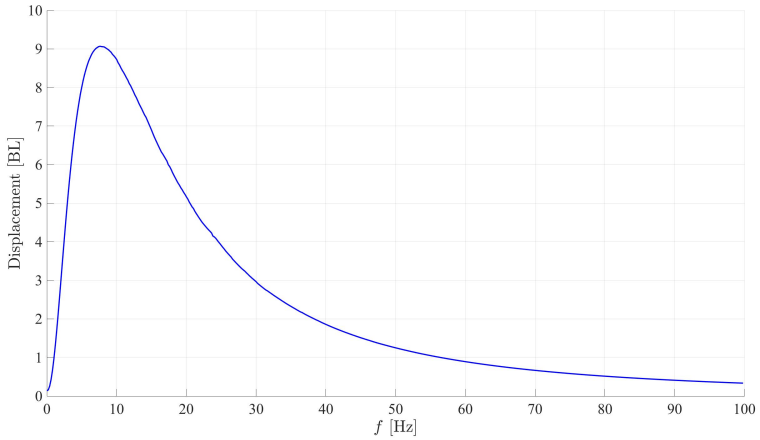

Figure 4.2: Displacement of the two link swimmer in 100s as a function of frequency

whenever $m_t^1 > m_t^2 > 0$. The individual links of the swimmer remain aligned with the constant component of the field demonstrating how the constant component acts like a magnetization spring that tries to stabilize the orientation of the two links around itself. Since the links have only longitudinal magnetizations, it is technically correct to refer to the orientation of the link as the orientation of the internal magnetic moment and vice versa. However, if the links did have lateral components as well, we would have to be more careful about the terminology. For these simulations, we achieved an average velocity of $v_{avg} = 0.092BL/s$. Additionally, for the same control inputs, we initialized the swimmer's orientation from several random configurations. The flows of the system state demonstrate that all these initial orientations converge to the same limit cycle in the (θ_1, θ_2) space as shown in Figure. 4.3. In Section 4.5, we will exploit this fact to demonstrate that this limit cycle is indeed sufficient to generate net displacement along X_w of the world.

Trajectory Tracking

From Figure 4.3, we notice that the limit cycle in the (θ_1, θ_2) has a large basin of attraction. This demonstrates that it is possible to align the swimmer with the external magnetic field even when the initial orientation of individual links of the swimmer is off by π radians relative to the direction of the constant component of the external field. The dual to this scenario is the case when the initial orientation of the swimmer is always along the world X_w axis while the constant component of the field changes direction. By symmetry arguments, it is possible to prove that both situations are equivalent. Hence, we can exploit this fact to make the swimmer translate along a given trajectory in the world by suitably switching the direction of the constant component and the oscillating component. For example, given a desired rectangular trajectory in the workspace as defined by the red track in Figure 4.5a, we can synthesize the switching time instants (t_1, t_2, t_3, t_4) and control inputs $\boldsymbol{u}(t)$ which make the swimmer to track this trajectory using Eq. 4.9

$$\boldsymbol{u}(t) = \begin{cases} \boldsymbol{u}_{trans}(t) & 0 \leq t \leq t_1 \\ R_{\frac{\pi}{2}} \boldsymbol{u}_{trans}(t) & t_1 < t \leq t_2 \\ R_{\pi} \boldsymbol{u}_{trans}(t) & t_2 < t \leq t_3 \\ R_{\frac{3\pi}{2}} \boldsymbol{u}_{trans}(t) & t_3 < t \leq t_4 \end{cases} \tag{4.9}$$

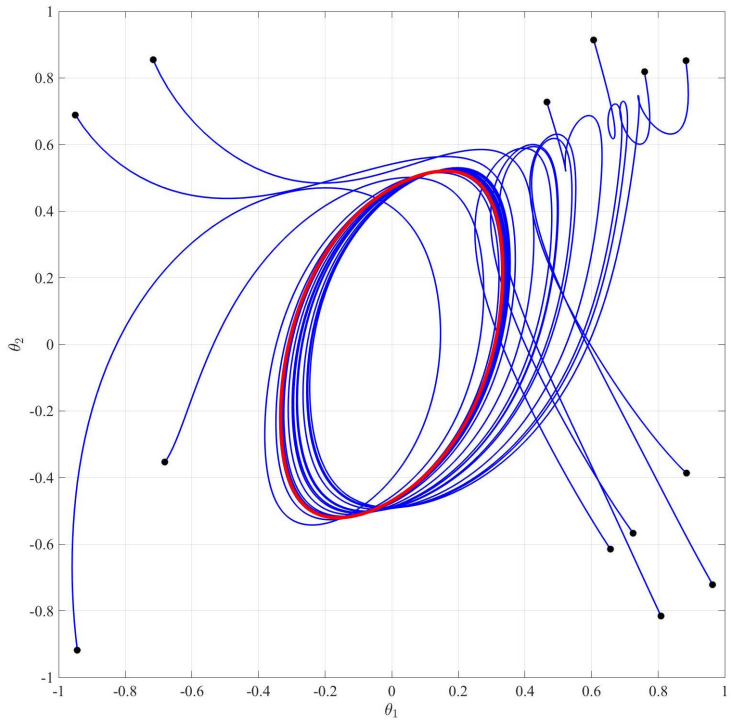

Figure 4.3: Limit cycle behavior of the (θ_1, θ_2) from different initial orientations using $B_x = 1, B_y = \sin \omega t$

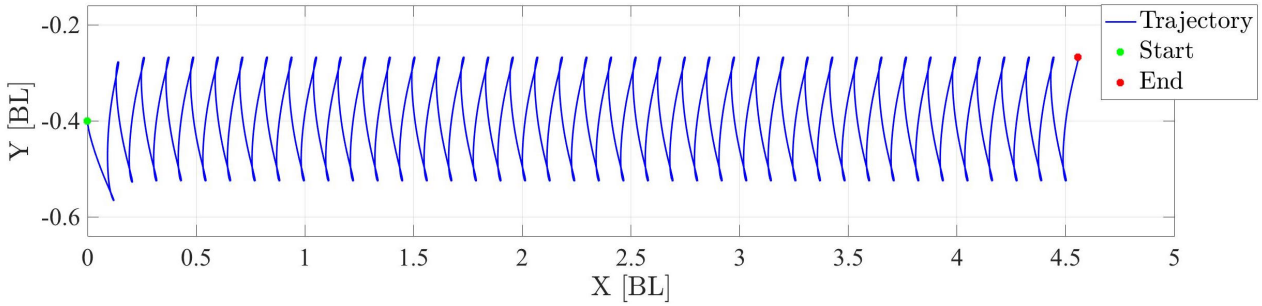

Figure 4.4: Translation Trajectory of the two-link swimmer with $B_x = 1, B_y = \sin \omega t$

For the example in Figure 4.5a, we can chose t_1, t_2, t_3, t_4 using the knowledge of the average velocity of the swimmer corresponding to the $\boldsymbol{u}_{trans}(t)$ primitive and the displacement of the swimmer in the desired trajectory during each piecewise defined interval. From Figure 4.5a, note that the swimmer exhibits a transient response when the control input switches. This behavior is expected as the swimmer uses this time to adjust the orientation of its links, with the new direction of the constant component of the external field. The corresponding limit cycles are shown in Figure 4.5b.

Tracing a circle

In the previous section, we demonstrated how translation along a desired trajectory in the world can be obtained by using discontinuous jumps in the control input (Eq. 4.9). Following a similar approach, we can can compose $\boldsymbol{u}_{trans} = (1, \sin \omega t)$ with a slower frequency component which rotates $\boldsymbol{u}_{trans}$ continuously and makes the swimmer track an arc of a circle (Figure. 4.6). This

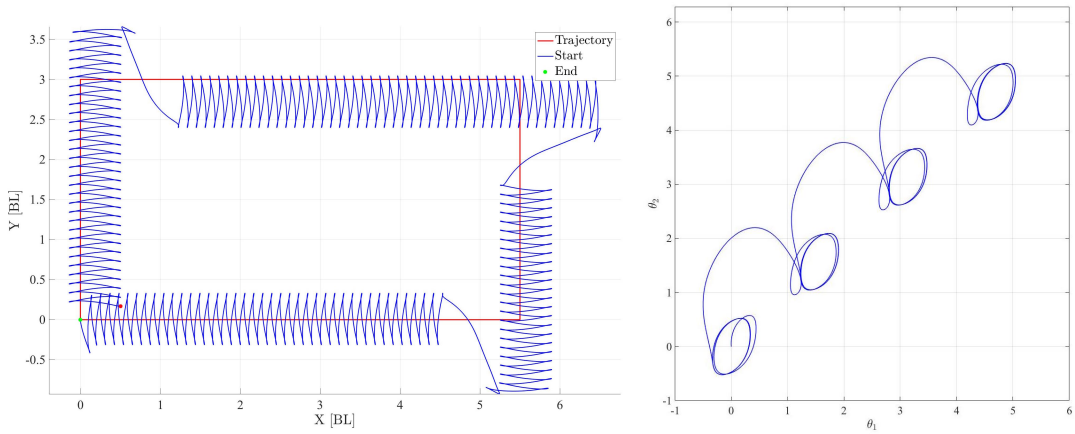

(a) Tracking a rectangular trajectory using piecewise defined magnetic fields

(b) Limit cycles in the (θ_1, θ_2) space corresponding to the rectangular trajectory

control input is described in Eq. 4.10

$$\boldsymbol{u}_{circle} = \begin{bmatrix} \cos\omega_{slow}t & -\sin\omega_{slow}t \\ \sin\omega_{slow}t & \cos\omega_{slow}t \end{bmatrix} \underbrace{\begin{bmatrix} 1 \\ \sin\omega t \end{bmatrix}}_{\boldsymbol{u}_{trans}} \tag{4.10}$$

where $\omega_{slow} < \omega$. The slow frequency is needed for the swimmer to accumulate some displacement along the instantaneous direction of the constant component of the field. Since the constant vector eventually goes through a full circle, the swimmer's trajectory also follows that cycle which results in a motion that traces the perimeter of a circle. In the figure on the left, we selected $\omega_{slow} = \frac{\omega}{20}$ and in the figure on the right $\omega_{slow} = \frac{\omega}{200}$. The purpose of this simulation is to demonstrate how a fast rotating $\boldsymbol{u}_{trans}$ does not result in significant translation and can be interpreted as resulting in a turning in place locomotion. On the other hand, choosing $\omega_{slow} = \frac{\omega}{200}$ allows the swimmer to advance forward while also causing it to turn, and the net effect results in the swimmer tracking a circle, as depicted in the figure on the right.

In addition to the control inputs presented here, we also considered simulating the response of the swimmer to fields with only constant components, fields with only sinusoidal components and fields with high amplitude sinusoids. The results from these simulations for different magnetization values are presented in Table 4.2. As is expected, for the case where the swimmer has complete front back symmetry with respect to magnetization (*i.e.* (1,1)), the swimmer undergoes no displacement for any control input. The small displacements the swimmer undergoes for sinusoids are periodic back and forth motions which average out to zero over a full cycle, thus resulting in zero net motion over a given number of cycles. The only significant motion experienced by the swimmer is when the magnetization is asymmetric *i.e.* $(1, 2)$ case and when the swimmer is excited with crossed uniform and oscillating fields as described in this section.

4.3.2 Trajectories with elastic effects

We now consider the case of the swimmer where elastic effects are also present *i.e.* $\kappa \neq 0$. The results of numerical simulations are summarized in Table 4.3. We describe key interesting results here:

For the case where the magnetizations are asymmetric (*i.e.* $\frac{m_i^2}{m_i^1} = 2$), the swimmer exhibits translational displacement under crossed oscillating and uniform fields like before as was expected

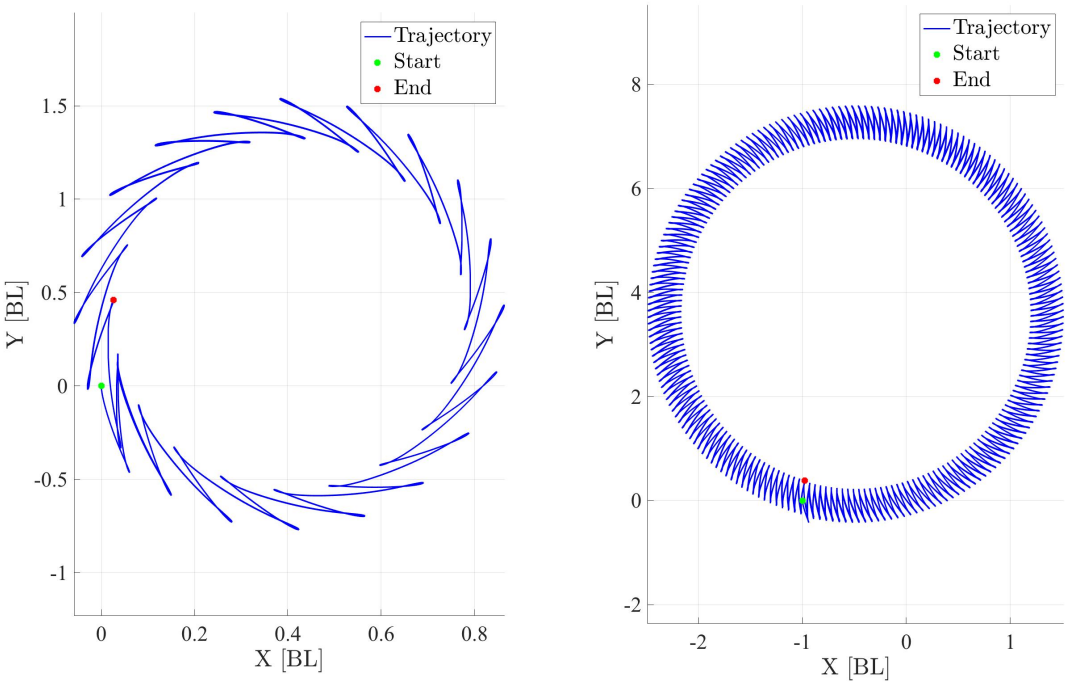

Figure 4.6: Trajectory of the two-link swimmer with $B_x = \cos\omega_{slow}t - \sin\omega_{slow}t\sin\omega t$, $B_y = \sin\omega_{slow}t + \cos\omega_{slow}t\sin\omega t$

Table 4.2: Translation of two link swimmer without spring under different inputs and magnetizations

Control Input \ Magnetization $(1, \frac{m_t^2}{m_t^1})$	(1,1)	(1,2)	(0,1)
$B_x = 1, B_y = \sin\omega t$	0.04	18.12	0.14
$B_x = 1, B_y = 0$	0	0	0
$B_x = 0, B_y = \sin\omega t$	0.013	0.104	0

based on condition 2 mentioned in the beginning of Section 4.3. Additionally, for the same magnetizations, we also get displacement when the constant component is switched off *i.e.* $B_x(t) = 0$ and the vertical component $B_y(t)$ is a high-amplitude sinusoid. Since the constant component is switched off, the swimmer tends to align its links with the oscillating component which changes in the vertical spatial direction. Therefore, the swimmer is executes a swing π radians. Nevertheless, the limit cycle behavior in this case indeed depends on the initial orientation of the internal magnetizations relative to the external field. This is because the attractive limit cycle will correspond to the one that is in some sense 'closest' to stabilize to. Since the external field vector exhibits a full π radians of swing, it can be tracked from either 'side' of the $\boldsymbol{B} = (0, 8\sin\omega t)$ vector at a given t . Based on geometric arguments, it can then be proven that the net translational displacement of the swimmer will also depend on the resulting limit cycle and hence on the initial orientation of the internal magnetizations relative to the external field. For the simulation in the table, we assumed $\theta(0) = (0, 0)$.

Secondly, the swimmer with $(0, 1)$ magnetization also undergoes displacement in $B_x = 1, B_y = \sin\omega t$ field as was expected from condition 3 in the beginning of Section 4.3. This is

because the nonmagnetic link is paired to the magnetic link via the torsional spring. Since the magnetic link is coupled to the external magnetic field via the virtual 'magnetization' spring, the non-magnetic link also indirectly becomes receptive to the 'magnetization' spring due to the torsional coupling. Hence, it exhibits undulations which tend to emulate the presence of magnetization even though it is magnetically passive. Although not as effective as the $(1, 2)$ case, this scenario can be used to transport a non-magnetic load with a single magnetic link as was explored in [19] and [2]. We can extend this case to transporting a cargo with two magnetic links which will be described in the simulations for the three link swimmer in the next section.

Table 4.3: Translation of two link swimmer with spring under different inputs and magnetizations

Control Input \ Magnetization $(1, \frac{m_t^2}{m_t^1})$	(1,1)	(1,2)	(0,1)
$B_x = 1, B_y = \sin \omega t$	0.26	17.12	2.4
$B_x = 1, B_y = 0$	0	0	0
$B_x = 0, B_y = \sin \omega t$	0.02	1.504	2.49
$B_x = 0, B_y = 8 \sin \omega t$	2.251	19	1.9

4.4 Three-link Swimmer Simulations

We now describe the trajectories resulting from the simulations of three link swimmer. As mentioned in Section 4.2.1, the dynamics of the three link swimmer are very similar to the two link swimmer with the difference being that in addition to the two orientations, we also have the orientation of the third link in the state. Therefore, some qualitative properties of the simulations can be readily explained based on the results from the two link swimmer. For example, whenever the three link swimmer possess front back symmetry *i.e.* $m_t^1 = m_t^3$, the swimmer does not undergo net translation. Similarly, when one of the links is non-magnetic, the swimmer is qualitatively similar to a two link swimmer with a nonmagnetic cargo. To keep the discussion brief, we have summarized the results in Tables 4.4 and 4.5. In the next section, we a systematic procedure that we used to compute the (m_t^1, m_t^2, m_t^3) which maximize the translation over a given cycle of the oscillating magnetic field.

Table 4.4: Translation of three link swimmer without spring under different inputs and magnetizations

Control Input \ Magnetization $(1, \frac{m_t^2}{m_t^1}, \frac{m_t^3}{m_t^1})$	(1,4.54,0)	(1,4.54,1)	(1,4.54,4.54)
$B_x = 1, B_y = \sin \omega t$	21.47	0.1	35.81
$B_x = 1, B_y = 0$	0	0	0
$B_x = 0, B_y = \sin \omega t$	0.133	0.03	0.02
$B_x = 0, B_y = 8 \sin \omega t$	3.48	2.4	1.56

Table 4.5: Translation of three link swimmer with spring under different inputs and magnetizations

Control Input \ Magnetization $(1, \frac{m_t^2}{m_t^1}, \frac{m_t^3}{m_t^1})$	(1,4.54,0)	(1,4.54,1)	(1,4.54,4.54)
$B_x = 1, B_y = \sin \omega t$	20.525	0.33	35.88
$B_x = 1, B_y = 0$	0	0	0
$B_x = 0, B_y = \sin \omega t$	2.68	0..260	3.054
$B_x = 0, B_y = 8 \sin \omega t$	21.69	2.06	2.713

4.4.1 Numerical optimization for magnetization constants

For the simulations in the previous section, we used $\frac{m_t^2}{m_t^1} = 4.54$ and $\frac{m_t^3}{m_t^1} = 4.54$. In this section, we explain a systematic approach to compute these numbers. From this section forth, we will assume that the magnetization of the first link is unit magnitude, whereas the magnetizations of link two relative to link one, and link three relative to link one are the optimization variables. Hence, we have two parameters $\gamma = \frac{m_t^2}{m_t^1}$ and $\beta = \frac{m_t^3}{m_t^1}$ that we are interested in computing. We will choose the objective function to be the displacement the swimmer undergoes per cycle of the external magnetic field. There are two methods of computing these values.

1. **Brute Force Optimization**: This technique would require us to sample these parameters $\gamma \in \mathcal{D}$ and $\beta \in \mathcal{D}$ from a large domain $\mathcal{D} = [0, 100]$. After randomly selecting these parameters, we forward simulate the system dynamics with these parameters for one cycle of the actuating field and record the forward displacement. Once we have a full database of

the forward displacement for several parameters, we can pick up the parameter from this lookup table that results in maximum displacement. It suffices to say that this technique is computationally expensive and does not scale easily to systems with more than three links.

2. **Function Optimization**: As a way to circumvent computationally expensive brute-force optimization, we resort to ideas from asymptotic approximations explored in [19]. The idea is to compute an approximate analytical solution to the differential equations governing the dynamics of the swimmer in parameters γ and β. Given this expression, it becomes easy to use off-the-shelf function optimization routines such as *fmincon*, to compute parameters that maximize this function. The numerical values $\frac{m_t^2}{m_t^1} = 4.54$ and $\frac{m_t^3}{m_t^1} = 4.54$ were computed using this method.

Consider the dynamics of the two-link swimmer without spring as follows:

$$\begin{aligned} \boldsymbol{q}(0) &= \begin{bmatrix} 0 & 0 & 0 & 0 \end{bmatrix}^T \\ \dot{\boldsymbol{q}} &= \boldsymbol{g}_1(\boldsymbol{q})B_x(t) + \boldsymbol{g}_2(\boldsymbol{q})B_y(t) \\ &= \boldsymbol{G}(\boldsymbol{q})\boldsymbol{u} \end{aligned} \tag{4.11}$$

where $\boldsymbol{q} = [x, y, \theta_1, \theta_2]$. For the function optimization, we will assume that the control input is prespecified *i.e.* $\boldsymbol{u}(t) = \boldsymbol{u}_{trans} = (1, w)$ where $w = \sin \omega t$, and the initial condition is fixed *i.e.* $\boldsymbol{q}(0) = \begin{bmatrix} 0 & 0 & 0 & 0 \end{bmatrix}^T$. This is important because the solutions to Eq. 4.11 depend on the control input and the initial conditions. We are interested in computing an approximate expression for forward displacement of the swimmer over one cycle. This corresponds to the x component of the state.

Additionally, since the links have magnetization along the length ($m_t^1 > 0, m_t^2 > 0, m_t^3 > 0$), and the constant component of the field is along the X_w axis of the world frame, it suffices to assume that the angles $\theta_1, \theta_2, \theta_3$ oscillate about 0 *i.e.* $\theta_i \in [-\theta_{max}, \theta_{max}]$ for $i \in \{1, 2, 3\}$. Moreover, if we scale the amplitude of $w \longrightarrow \epsilon w$, where $\epsilon \ll 1$, we would expect that $\theta_{max} \longrightarrow 0$. Hence, we can approximate the solution to Eq. 4.11 with $\boldsymbol{u} = (1, \epsilon w)$ using the following Taylor series

$$\boldsymbol{q}(t) = \boldsymbol{q}^{(0)}(t) + \epsilon \boldsymbol{q}^{(1)}(t) + \epsilon^2 \boldsymbol{q}^{(2)}(t) + \cdots \tag{4.12}$$

and the corresponding derivatives become:

$$\dot{\boldsymbol{q}}(t) = \dot{\boldsymbol{q}}^{(0)}(t) + \epsilon \dot{\boldsymbol{q}}^{(1)}(t) + \epsilon^2 \dot{\boldsymbol{q}}^{(2)}(t) + \cdots \tag{4.13}$$

Now, we can compute simplified expressions for $\boldsymbol{q}(t)$ using leading order terms $\boldsymbol{q}_0, \boldsymbol{q}_1, \boldsymbol{q}_2$. It turns out $\boldsymbol{q}^{(0)}(t) \equiv 0$ because when the oscillating component of the magnetic field is off (*i.e.* $\epsilon = 0$) and the swimmer initially is at $\boldsymbol{q}(0) = \begin{bmatrix} 0 & 0 & 0 & 0 \end{bmatrix}^T$, it persists to stay in that state. Additionally, the $\dot{x}^{(1)}$ and $\dot{y}^{(1)}$ dynamics of the first order terms $\boldsymbol{q}^{(1)}(t)$ turn out to be identically zero from calculations, whereas the dynamics for $\theta_1^{(1)}(t)$, $\theta_2^{(1)}(t)$, $\theta_3^{(1)}(t)$ are nonzero. Hence, we need only compute second order terms $x^{(2)}$ and $y^{(2)}$ as a function of t . Finally, we notice that since the expressions for $\boldsymbol{g}_1(\boldsymbol{q})$ and $\boldsymbol{g}_2(\boldsymbol{q})$ depend only on the orientation variables $\theta_1, \theta_2, \theta_3$, we can first compute leading order solutions for $\theta_1, \theta_2, \theta_3$ *i.e.* $\theta_1^{(1)}(t)$,$\theta_2^{(1)}(t)$, $\theta_3^{(1)}(t)$ and use those expressions to then compute solutions for the $x^{(2)}(t)$ and $y^{(2)}(t)$ components of the state. In this process, we have ignored the second order terms corresponding to orientation variables *i.e.*

$\theta_1^{(2)}(t)$,$\theta_2^{(2)}(t)$, $\theta_3^{(2)}(t)$. Hence, we now write the dynamics for the θ components using Eq. 4.11.

$$\begin{aligned}\boldsymbol{\theta}(0) &= \begin{bmatrix}0 & 0 & 0\end{bmatrix}^T \\ \dot{\boldsymbol{\theta}} &= \boldsymbol{f}(\boldsymbol{\theta}, w) = \boldsymbol{f}_1(\boldsymbol{\theta}) + \boldsymbol{f}_2(\boldsymbol{\theta})w\end{aligned}$$

The dynamics for first order terms $\theta_1^{(1)}(t)$,$\theta_2^{(1)}(t)$, $\theta_3^{(1)}(t)$ can be written as a linear dynamical system as follows.

$$\dot{\boldsymbol{\theta}}^{(1)} = A\boldsymbol{\theta}^{(1)} + Bw \tag{4.14}$$

where

$$\begin{aligned}A &= \left.\frac{\partial \boldsymbol{f}}{\partial \boldsymbol{\theta}}\right|_{(\boldsymbol{\theta},w)=(\mathbf{0},0)} = \left.\frac{\partial \boldsymbol{f}_1}{\partial \boldsymbol{\theta}}\right|_{(\boldsymbol{\theta},w)=(\mathbf{0},0)} \\ B &= \left.\frac{\partial \boldsymbol{f}}{\partial w}\right|_{(\boldsymbol{\theta},w)=(\mathbf{0},0)} = \boldsymbol{f}_2(\mathbf{0})\end{aligned} \tag{4.15}$$

For a sinusoid input $w = \sin\omega t$, the solution to this system is

$$\boldsymbol{\theta}^{(1)}(t) = \boldsymbol{C}(\gamma,\beta)\sin\omega t + \boldsymbol{D}(\gamma,\beta)\cos\omega t \tag{4.16}$$

where $\boldsymbol{C} \in \mathbb{R}^3$ and $\boldsymbol{D} \in \mathbb{R}^3$. We have explicity shown the dependence of $\boldsymbol{C}$ and $\boldsymbol{D}$ on the magnetization parameters γ, β. The dynamics for the x component can be invoked from Eq. 4.11 as

$$\begin{aligned}x(0) &= 0 \\ \dot{x} &= h(\boldsymbol{\theta}, w) = h_1(\boldsymbol{\theta}) + h_2(\boldsymbol{\theta})w\end{aligned}$$

The second order dynamics for $x^{(2)}(t)$ can be written as follows:

$$\dot{x}^{(2)}(t) = 0.5\sum_{i=1}^{3}\left.\frac{\partial^2 h}{\partial\theta_i^2}\right|_{(\mathbf{0},0)}\theta_i^2 + \sum_{i\neq j}^{3}\left.\frac{\partial^2 h}{\partial\theta_i\partial\theta_j}\right|_{(\mathbf{0},0)}\theta_i\theta_j + \sum_{i=1}^{3}\left.\frac{\partial^2 h}{\partial\theta_i\partial w}\right|_{(\mathbf{0},0)}\theta_i w + 0.5\left.\frac{\partial^2 h}{\partial w^2}\right|_{(\mathbf{0},0)}w^2 \tag{4.17}$$

Finally, substituting Eq. 4.16 in Eq. 4.17 and integrating Eq. 4.17 over one cycle $T = \frac{2\pi}{\omega}$ gives an analytic expression of $x(T) = f(\gamma,\beta,\omega)$. We use this analytic expression in *fmincon* for $\gamma, \beta \in \mathcal{D}$ and compute the the optimum γ^*, β^* values. For more details we refer the reader to the supplementary materials provided in [19]. To illustrate the power of this method, we show a comparison of the per cycle displacement of the swimmer as function to the frequency using full numerical simulations and this approximate expression. For this simulation, we chose the magnetization parameters γ and β arbitrarily. As can be seen from the graph, the solution using asymptotic methods is a very good approximation to the true numerical solution. In Section 4.6.2, we describe the procedure to encode these magnetizations in elastomagnetic filaments.

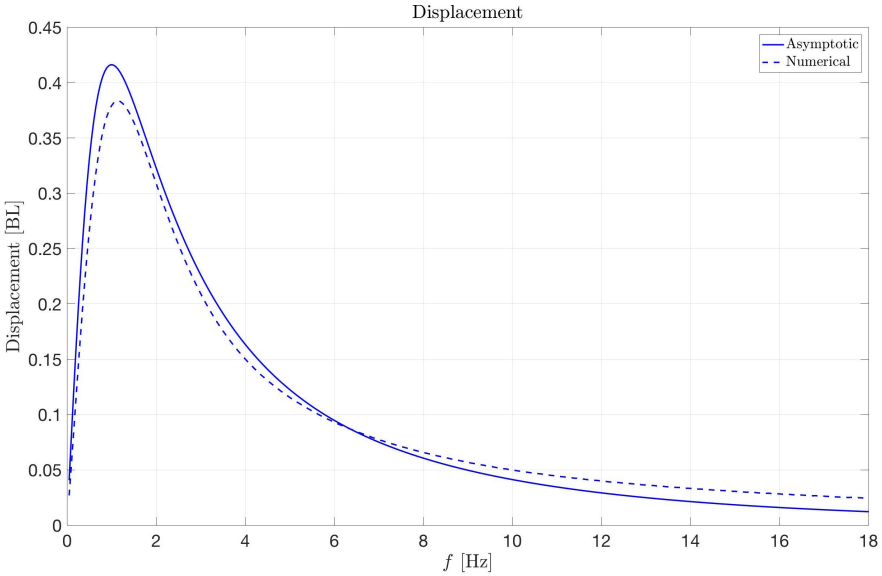

Figure 4.7: Comparison of three swimmer displacement v/s frequency using asymptotic method and exact numerical simulations. For this simulation $\gamma = 2, \beta = 3$ were chosen arbitrarily

4.5 Geometric approach to synthesizing motion plans

In the previous sections, we demonstrated that the existence of the limit cycle in the (θ_1, θ_2) portrait was related to the net translation of the swimmer. Indeed, for the rectangular trajectory, we noted that the direction of the swimmer's net motion was correlated with the external magnetic field's constant component, and whenever the direction switched by $\frac{\pi}{2}$, the corresponding limit cycle also changed. Additionally, as we noted in the turn in place motions, the the (θ_1, θ_2) cycle was continuously evolving which prevented the swimmer to accumulate net displacement along one direction, instead causing it to turn in place. From these simulations, we can conclude that existence of a periodic limit cycle is necessary to accumulate displacement. In this section, we give a mathematical proof for why such a limit cycle exists and additionally, why it results in displacement. We resort to arguments developed in Chapter 3 of this thesis and demonstrate that the limit cycle can be interpreted as a 'gait'. While technically the limit cycle is not a periodic internal shape change, the resulting arguments can still be extended to periodic trajectories in the orientation angle space. We will only consider the case where the swimmer does not have a spring, as the driftlessness of the dynamics is essential to the ensuing development.

4.5.1 Decoupling system dynamics

Consider the differential equations governing the dynamics of the two link swimmer (Eq. 4.18).

$$\begin{aligned} \dot{\boldsymbol{q}} &= \boldsymbol{g}_1(\boldsymbol{q})B_x(t) + \boldsymbol{g}_2(\boldsymbol{q})B_y(t) \\ &= \boldsymbol{G}(\boldsymbol{q})\boldsymbol{u} \end{aligned} \tag{4.18}$$

where $\boldsymbol{q} = (x, y, \theta_1, \theta_2)$, $\boldsymbol{G}(\boldsymbol{q}) = [\boldsymbol{g}_1(\boldsymbol{q}), \boldsymbol{g}_2(\boldsymbol{q})]$, $\boldsymbol{u} = (B_x(t), B_y(t))$. We know that since the magnetic field is spatially uniform, the (x, y) position coordinates do not have an effect on the swimmer's motion. The only state variables that influence the dynamics the orientation of the swimmer's links with respect to the external magnetic field. Therefore, the dynamics of the position variables *i.e.* $\dot{\boldsymbol{p}}$ exclusively depend on the orientation variables (θ_1, θ_2). Similarly, the dynamics of the orientation variables $(\dot{\theta}_1, \dot{\theta}_2)$ also depend exclusively on (θ_1, θ_2). Hence, we can

break Eq. 4.18 into two separate sub-systems as follows:

$$\begin{aligned}
\dot{\boldsymbol{q}} &= \boldsymbol{G}(\boldsymbol{q})\boldsymbol{u} = \boldsymbol{G}(\boldsymbol{\theta})\boldsymbol{u} \\
\implies \begin{bmatrix}\dot{\boldsymbol{p}} \\ \dot{\boldsymbol{\theta}}\end{bmatrix} &= \begin{bmatrix}\boldsymbol{P}(\boldsymbol{\theta}) \\ \boldsymbol{H}(\boldsymbol{\theta})\end{bmatrix}\boldsymbol{u} \\
\implies \dot{\boldsymbol{p}} &= \boldsymbol{P}(\boldsymbol{\theta})\boldsymbol{u} \qquad (4.19) \\
\dot{\boldsymbol{\theta}} &= \boldsymbol{H}(\boldsymbol{\theta})\boldsymbol{u} \qquad (4.20)
\end{aligned}$$

where $\boldsymbol{P}(\boldsymbol{\theta}) \in \mathbb{R}^{2\times 2}$ and $\boldsymbol{H}(\boldsymbol{\theta}) \in \mathbb{R}^{2\times 2}$. Assuming $\boldsymbol{H}(\boldsymbol{\theta})$ is invertible on $[-2\pi, 2\pi] \times [-2\pi, 2\pi]$, we can compute $\boldsymbol{u}$ from Eq. 4.20 and substitute in 4.19 as follows:

$$\begin{aligned}
\boldsymbol{u} &= \boldsymbol{H}^{-1}(\boldsymbol{\theta})\dot{\boldsymbol{\theta}} \qquad (4.21a) \\
\implies \dot{\boldsymbol{p}} &= \boldsymbol{P}(\boldsymbol{\theta})\boldsymbol{H}^{-1}(\boldsymbol{\theta})\dot{\boldsymbol{\theta}} \qquad (4.21b) \\
\implies \dot{\boldsymbol{p}} &= \boldsymbol{J}(\boldsymbol{\theta})\dot{\boldsymbol{\theta}} \qquad (4.21c) \\
\implies \begin{bmatrix}\dot{x} \\ \dot{y}\end{bmatrix} &= \begin{bmatrix} j_{11}(\theta_1,\theta_2) & j_{12}(\theta_1,\theta_2) \\ j_{21}(\theta_1,\theta_2) & j_{22}(\theta_1,\theta_2)\end{bmatrix}\begin{bmatrix}\dot{\theta}_1 \\ \dot{\theta}_2\end{bmatrix} \qquad (4.21d)
\end{aligned}$$

where $\boldsymbol{J}(\boldsymbol{\theta}) = \boldsymbol{P}(\boldsymbol{\theta})\boldsymbol{H}^{-1}(\boldsymbol{\theta})$. Note that Eq. 4.21c is in a form similar to the kinematic reconstruction equation (Eq.). However, note that in Eq. 4.21c the variables (θ_1, θ_2) refer to the orientation of the swimmer relative to the world. They are indeed not internal shape variables (which in this case would be $\alpha = \theta_2 - \theta_1$). Additionally, the left hand side of Eq. 4.21c also involves fiber velocities referenced relative to the inertial frame as opposed to the body velocities ξ expressed in the body frame. Hence, we cannot model the problem with a principal fiber bundle structure as in the case of the planar and 3D internally actuated swimmers. Nevertheless, assuming for the moment that we can fully and independently control (θ_1, θ_2), it is possible to compute the total displacement over a cyclic change in (θ_1, θ_2) as follows:

$$\begin{aligned}
\boldsymbol{p}(T) &= \int_0^T \boldsymbol{p}(t)dt \\
&= \int_0^T \boldsymbol{J}(\boldsymbol{\theta})\dot{\boldsymbol{\theta}}dt \\
&= -\int_\gamma \boldsymbol{J}(\boldsymbol{\theta})d\boldsymbol{\theta} \\
&= -\iint_{\mathcal{S}} \text{curl } \boldsymbol{J}\ d\theta_1 d\theta_2. \qquad (4.22)
\end{aligned}$$

In Eq. 4.22, we have used Stokes' theorem to simplify the problem of computing line integral of the rows of $\boldsymbol{J}(\boldsymbol{\theta})$ along (θ_1, θ_2) curves, to computing volume integrals defined over loops in (θ_1, θ_2). Just like in the case of internally actuated 3D swimmer, we can now compute loops in the (θ_1, θ_2) space to get a desired displacement of the swimmer in the world. Note however, that since the left hand side of Eq. 4.22 gives the displacement in the world frame directly, we do not have to worry about the discrepancy in the body velocity integral and the displacement in the world. To illustrate this point further, we plot the curl of x and y components of curl $\boldsymbol{J}(\theta_1, \theta_2)$ in Figure. 4.8. Additionally, we also superimpose the limit cycle (white) that results from exciting the two link swimmer with crossed uniform and oscillating magnetic fields from Section. 4.3. As one can notice, the white loop covers a net positive area in the x component of the curl $\boldsymbol{J}(\theta_1, \theta_2)$ whereas it encloses a zero area in the y component of curl $\boldsymbol{J}(\theta_1, \theta_2)$. Hence, one can argue that the swimmer undergoes a net translation in the X_w axis along the world, consistent with the results from numerical simulations in Section 4.3.

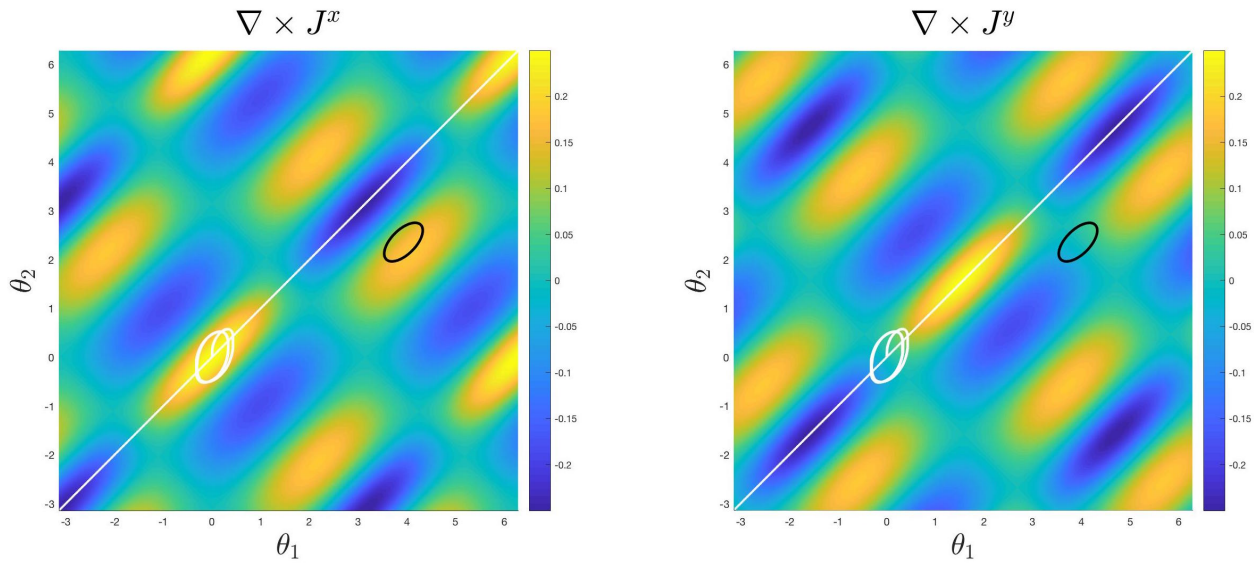

Figure 4.8: curl $\boldsymbol{J}$ computed over a $[-\pi, \pi] \times [-\pi, \pi]$ range for the magnetic swimmer. The white loop illustrates the limit cycle behavior that results from applying $\boldsymbol{u}_{trans} = (1, \sin \omega t)$ to two link magnetic swimmer. The loop in black is a candidate loop that also results in translation along X_w axis

4.5.2 Novel motion primitives

One can extend this tool to synthesizing new control inputs that also result in translation along X_w axis in the world. To that end, consider a time parametrized loop in the (θ_1, θ_2) defined as below:

$$\theta_1^d(t) = 0.5 \cos \omega t \cos \frac{\pi}{4} - 0.25 \sin \omega t \sin \frac{\pi}{4} + \frac{5\pi}{4} \tag{4.23a}$$

$$\theta_2^d(t) = 0.5 \cos \omega t \sin \frac{\pi}{4} + 0.25 \sin \omega t \cos \frac{\pi}{4} + \frac{3\pi}{4} \tag{4.23b}$$

This loop is depicted in black in Figure. 4.8. As one can notice, like the white loop, this loop is also a candidate trajectory that should result in net translation of the swimmer along X_w axis in the world. Using this parametrization, it is possible to compute a control law using Eq. 4.21a which is computed point-wise in time:

$$\boldsymbol{u}(t) = \boldsymbol{H}^{-1}(\theta_1^d(t), \theta_2^d(t)) \begin{bmatrix} \dot{\theta}_1^d \\ \dot{\theta}_2^d \end{bmatrix} \tag{4.24}$$

We can then simulate the full system dynamics using this control law. The resulting displacement of the swimmer is shown in Figure 4.9. As can be noticed from the figure, the swimmer indeed undergoes translation along X_w axis in the world. Note that central to do designing control inputs using this technique was the assumption that the matrix $\boldsymbol{H}$ be invertible. However, we notice that $\boldsymbol{H}(\boldsymbol{\theta})$ loses rank whenever the swimmer instantaneously passes through the straightened configuration *i.e.* $\theta_1 = \theta_2$ as shown in Figure 4.8. We circumvented this problem in defining the desired (θ_1, θ_2) trajectory to be away from this singularity.

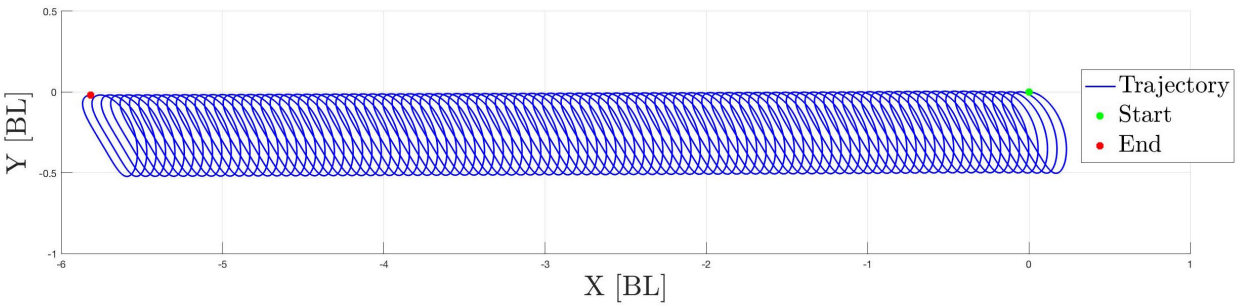

Figure 4.9: Translation of the two link swimmer corresponding to the magnetic fields computed using Eq. 4.24 for the trajectory defined in Eq. 4.23a-4.23b

4.6 Experimental Results

4.6.1 Design of the setup

Figure 4.10 gives a solidworks schematic of the setup. The workspace is surrounded by four coils. Since our swimmers our planar, we require a planar magnetic field *i.e.* it should have two components $\boldsymbol{B}(t) = (B_x(t), B_y(t))$. We use two pairs of Helmholtz coils to generate the magnetic fields. Coils from Pair 1 generate magnetic field in X_w direction whereas coils from Pair 2 generate magnetic field in the Y_w direction. We use two Roboclaw motor drivers to regulate the current through each pair. Using these drivers, we are able to command a desired mathematical function of the required magnetic field at the center of the workspace. We used a magnetometer to calibrate the current input to the coils with the generated magnetic field. This calibration was ultimately reverse engineered to compute inputs to the drivers that will generate a desired temporal field profile at the center of the workspace. Feedback information is provided by a top view camera (Logitech C920). The coil system is able to generate a nearly uniform magnetic field ($\sim$ 200 Gauss) in the small region in the workspace in arbitrary planar directions.

4.6.2 Swimmer Fabrication

We follow the procedure outlined in [12] to design elastomagnetic swimmers. However, instead of encoding continuously distributed magnetization profiles in a continuum flexible swimmer, we focus on magnetizations in individual links since we are interested in discrete swimmers. The swimmer is fabricated by patching two/three elastomagnetic links with non-magnetic elastomer. The patch constituting the bond between two links is flexible and it emulates the presence of a torsional spring. Each individual elastomagnetic link is made using a mixture of equal parts of unmagnetized ferromagnetic particles MQFP-B(D50=15μm) and Ecoflex 00-40 elastomer. The resulting mixture is poured in molds of size 10 mm $\times$ 4 mm $\times$ 2 mm and allowed to cure for a period of three hours.

The next step in the procedure is to encode the desired magnetization profile in the swimmer. To be consistent with numerical simulations, we only encode longitudinal magnetization profiles *i.e.* magnetization along the length of the link. We first describe the general procedure of how to magnetize a single link, and then describe how to ensure a desired ratio of internal magnetizations between consecutive links to respect the front back asymmetry.

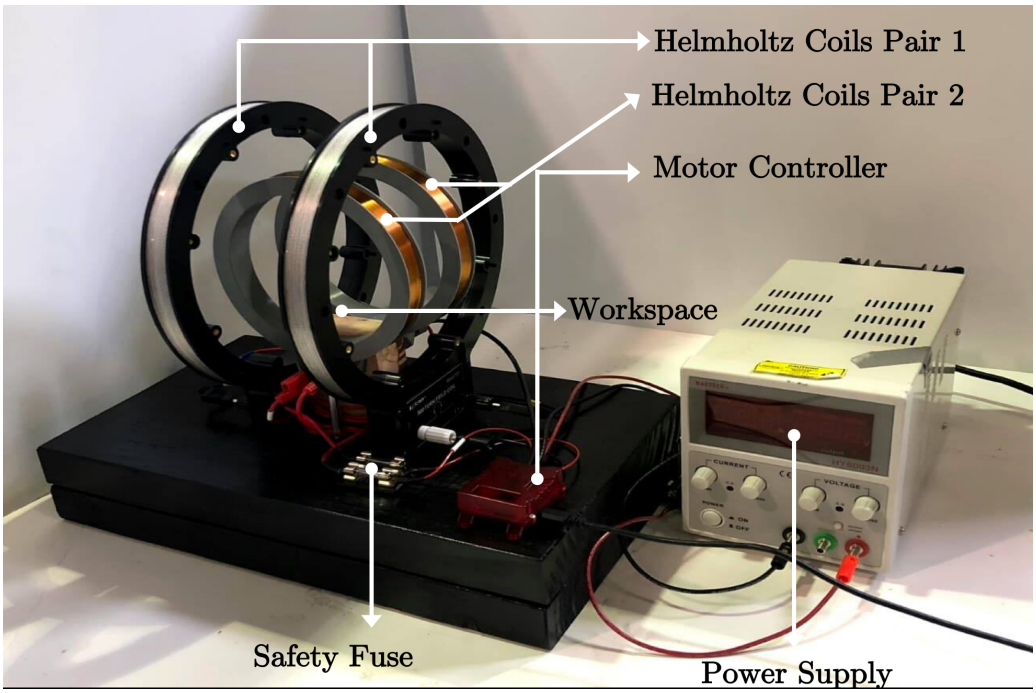

Figure 4.10: Illustration of the experimental setup used to generate planar magnetic fields

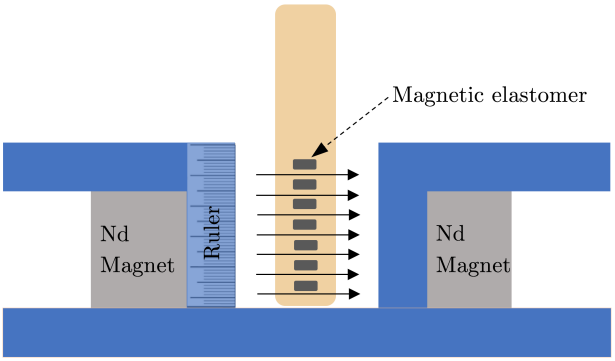

Figure 4.11: Schematic of the setup that generates $H = 0.6$ T field for programming the magnetization profiles in magnetic elastomers

General Procedure:

We use a pair of strong neodymium magnets facing each other to generate a strong magnetizing field to magnetize these a single link (see Figure. 4.11). Each link is suspended in the region between these magnets at a suitable level and left for 24 hours to allow sufficient time for magnetic domains to align unidirectionally. We assume that the strength of the magnetization induced inside the elastomer M is directly proportional to the strength of the field at the particular height in the space between the two magnets. We use a magnetometer to calibrate the strength of the magnetic field between the two neodymium magnets against the height at which the sensor is placed. This graph is depicted in Figure. 4.12. As can be seen, the variance in the magnetic field over a height of 3 cms is very large, which warrants careful placement of the single at the correct height.

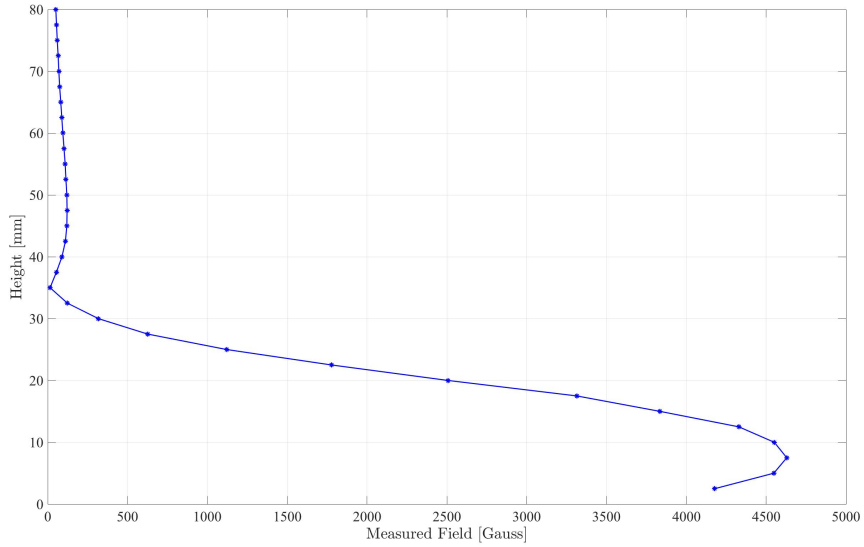

Figure 4.12: Distribution of magnetic field inside the magnetization setup as a function of height (see Fig. 4.11)

Breaking front-back magnetic symmetry :

In this section, we describe a principled approach to program a desired ratio magnetization profiles in individual links of the swimmers. As was demonstrated through numerical simulations in Section 4.3, the two link and three link swimmers are capable of undergoing net displacement only when the front back symmetry is broken *i.e.* $m_t^1 \neq m_t^2$ for the two link case and $m_t^1 \neq m_t^3$ for the three link case. While in simulation it is easy to set these numbers to arbitrary values, here we describe a systematic procedure to encode these ratios in the elastomagnetic swimmers. To illustrate the idea, we recall the model of a single link magnetic swimmer. Using Eq. 4.4, we can expand the dynamics as:

$$\begin{bmatrix} \dot{x} \\ \dot{y} \\ \dot{\theta} \end{bmatrix} = \frac{1}{T_m} \begin{bmatrix} 3\cos^2\theta \\ 1.5\sin 2\theta \\ -6\sin\theta \end{bmatrix} B_x(t) + \frac{1}{T_m} \begin{bmatrix} 1.5\sin 2\theta \\ -3\cos^2\theta \\ 6\cos\theta \end{bmatrix} B_y(t) \tag{4.25}$$

where $T_m = \frac{\xi L^2}{MB}$ is the magneto-viscous time scale. We will consider the solutions to Eq. 4.25 with initial conditions $\theta(0) = 0$ under the effect of the field $B_x(t) = 0$ and $B_y(t) = 1$. We are interested in investigating the time the swimmer takes to turn to align itself with the magnetic field as a function of the internal magnetization. Intuitively, the time the link takes to turn to align itself with the external field should be inversely related to the internal magnetization as a stronger magnet should respond faster. Hence the turning time can give us a good metric to compare the relative strengths of two magnets, which can ultimately be used to verify the ratios needed between two links of the magnetic swimmer.

For $\theta(0) = 0, B_x(t) = 0, B_y(t) = 1$, the differential equations have an analytical solution given by

$$\theta(t) = 2\tan^{-1}\left(\tanh\left(\frac{3t}{T_m}\right)\right) \tag{4.26}$$

From this solution, we can see that eventually the link will align with the magnetic field *i.e.* as $t \longrightarrow \infty$, $\theta(t) \longrightarrow \frac{\pi}{2}$. Instead, there is a finite time in which the link will be close to $\frac{\pi}{2}$. From

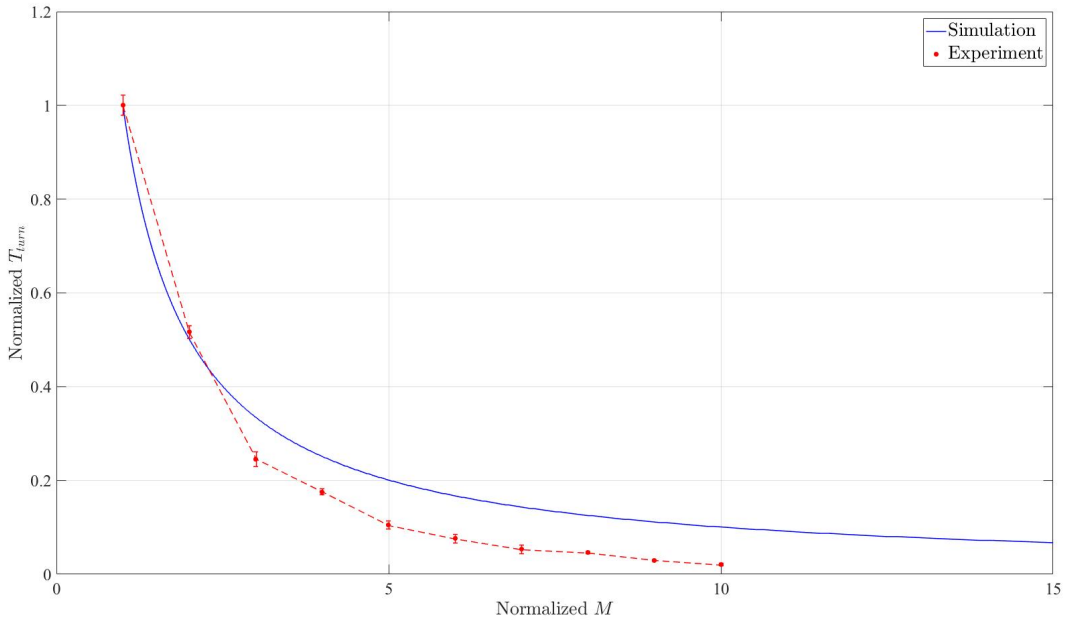

Figure 4.13: Turning time as a function of internal link magnetization. The blue curve is from simulations while the red curve is from experimental data.

the analytical solution, one can easily compute that the time to turn $T_{turn} \propto \frac{1}{M}$. Figure. **??** depicts the dependence of the time to turn by $\frac{\pi}{2}$ as predicted from simulations (blue) and as determined from experiments (red). From the graph, one can verify that indeed the time to turn varies inversely internal magnetization. Hence, this test can be used to compare internal magnetizations of two links. Once we identify two links with different magnetizations such as in the ratio of 1:2, we patch them together with an elastomeric bond which results in the complete swimmer. From numerical simulations, we know for the two link swimmer that as $\frac{m_t^2}{m_t^1}$ increases, the per cycle displacement of the swimmer increases until it saturates. To verify this, we conducted experiments with three different swimmers with internal magnetizations in the ratio of 1:2,1:3 and 1:4. In these experiments, the control input $\boldsymbol{u}_{trans}(t)$ was applied for a total duration of 200 cycles. Figure 4.14 depicts the displacements of the swimmer for these different magnetizations and it is evident from the figure that increasing the $\frac{m_t^2}{m_t^1}$ increases the total distance traveled. In subsequent sections, we will demonstrate our results of translation and turning in place using a two link swimmer with $\frac{m_t^2}{m_t^1} = 4$

Results for translation

We now present our results from applying $\boldsymbol{u}_{trans}(t) = B_0(1, \sin\omega t)$. For these experiments, we used $B_0 = 30$ Gauss and $\omega = 2\pi$rad/s. The swimmer was placed in the center of the workspace where the field is approximately uniform. Then, we powered the coils which creates constant field along X_w direction and sinusoidal in Y_w. This was done by supplying time varying current to the coils. The plot shown in Figure 4.15 depicts the translation of the tail of the two link swimmer. These points were hand tracked using *Tracker: Video Analysis and Modeling Tool*. As can be seen from the plot, the y component of the tail exhibits oscillations where as the x component is monotonically increasing. We limited the duration of the experiment because the region in which the swimmer is submerged does not have fully uniform magnetic field. Hence, as

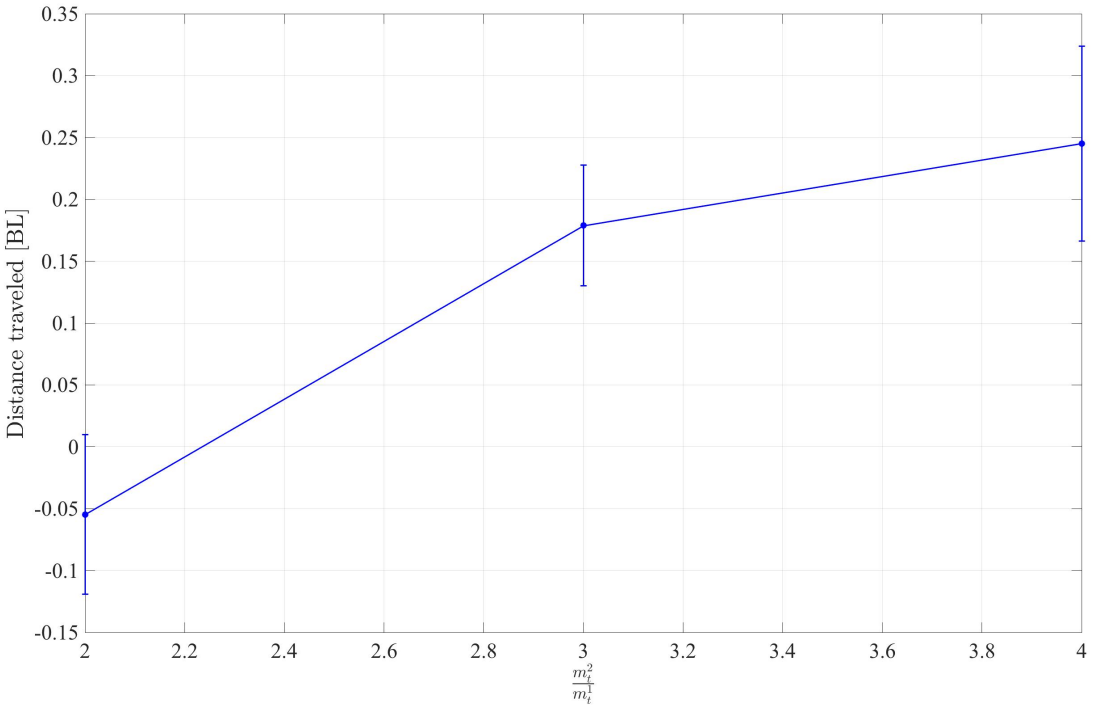

Figure 4.14: Distance traveled by three magnetic swimmers as a function of internal magnetization ratios under $B = 30$ Gauss

the swimmer comes closer to the coils, eventually, the effect of force gradients starts to dominate which creates an acceleration.

Results for turning in place

In this section, we depict the results of turning in place on the two link swimmer. For these experiments, we used $\boldsymbol{u}_{rot} = R_{\omega_{slow}t}\boldsymbol{u}_{trans}(t)$. The oscillating field frequency was still 1 Hz. We considered two different frequencies for the slow rotation *i.e.* $\omega^1_{slow} = \frac{\omega}{10}$ and $\omega^2_{slow} = \frac{\omega}{100}$. The corresponding graphs from the locomotion are shown in Figure 4.16. In the Figure on the left, the tail of the swimmer traces a circle. However, the undulations in the tip of the tail are not as pronounced.

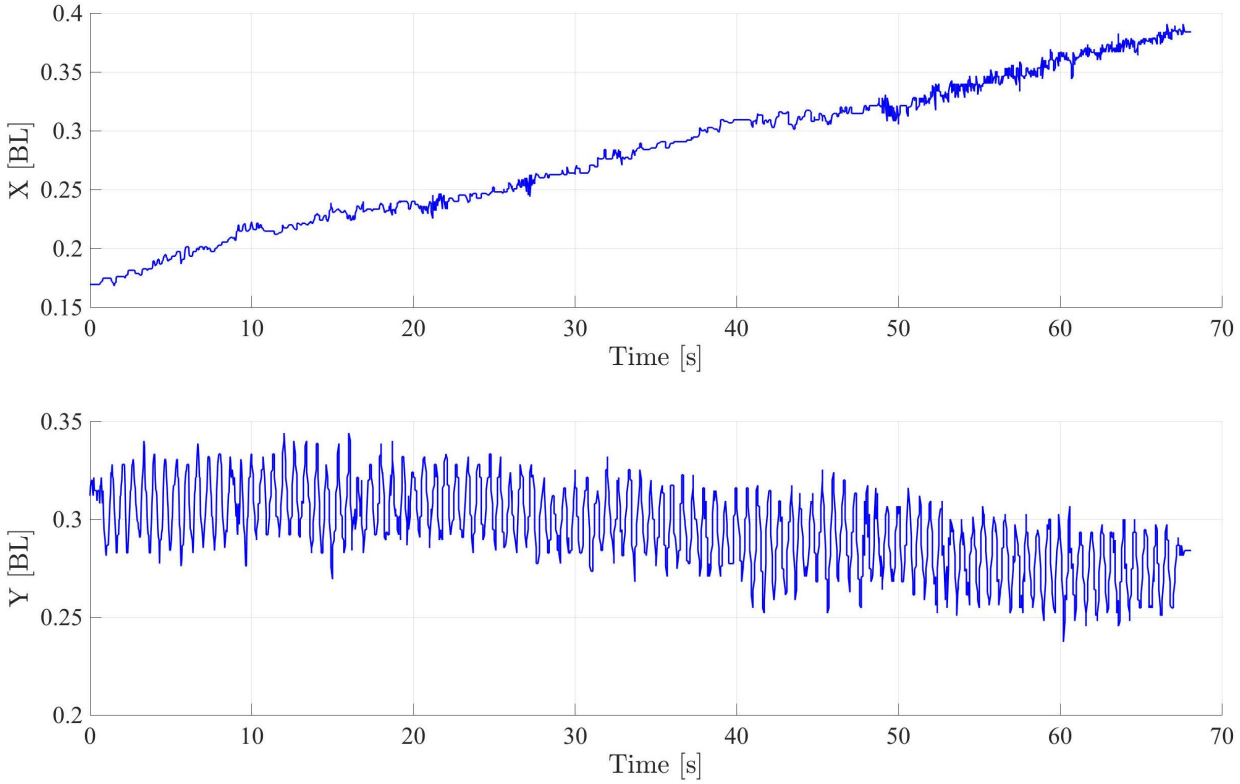

Figure 4.15: x and y components of the trajectory of the two-link swimmer under $\boldsymbol{u}_{trans}(t) = B_0(1, \sin \omega t)$

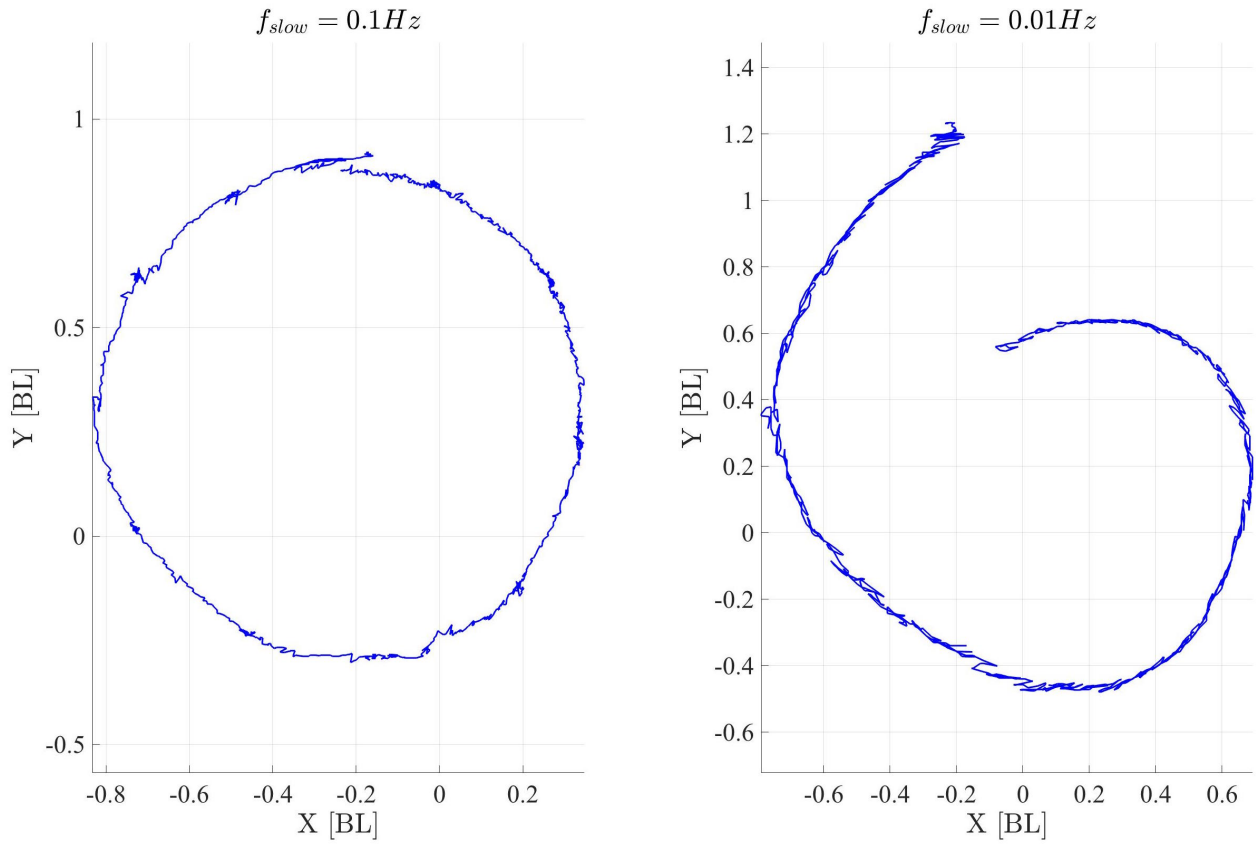

Figure 4.16: x and y components of the trajectory of the two-link swimmer under $\boldsymbol{u}_{rot} = R_{\omega_{slow}t}\boldsymbol{u}_{trans}(t)$ for $\omega_{slow} = 0.1(2\pi), 0.01(2\pi)$ rad/s

Chapter 5

Conclusions and Future Work

In this thesis, we explored motion planning methods for two different types of swimmers in the low-Re regime. We developed a mathematical model for a novel 3D swimmer and demonstrated how using tools from geometric mechanics, we can synthesize motion primitives for this swimmer that make it swim along a desired direction in the world. We also considered a planar elastomagnetic swimmer, which was actuated using external magnetic fields. Due to this form of actuation, we are unable to pose a reconstruction equation for this system. However, we demonstrated that the special case of the two link swimmer is amenable to control synthesis using similar geometric methods that were leveraged for gait synthesis for internally actuated swimmers.

As an extension to these results, we would naturally like to extend these tools to designing control inputs for three link magnetic swimmers and beyond. Although prior work has demonstrated that numerical optimization and knowledge of backbone curves in snakes can be leveraged to simplify geometric gait synthesis for internally actuated 'N' link snake robots, these techniques cannot easily be extended to 'N' link magnetic swimmers. This is because the magnetization constants in the links enforce a constraint on how links bend relative to one another and hence a template serpenoid curve cannot be fitted without reasoning about internal magnetizations. In the internally actuated robots, direct command over internal joint variables provides the freedom to follow any backbone curve which reduces the dimensionality of the gait synthesis problem. However, the process of reducing dimensionality for an 'N' link magnetic swimmer requires reasoning about internal magnetizations as well.

Additionally, we would like to investigate stability properties of the limit cycles that result from applying crossed uniform and transverse oscillating fields to the two link swimmer. As we verified numerically, the two link magnetic swimmer has a large basin of attraction. However, the stability properties of this limit cycle change depending on the relative internal magnetizations between links. Hence, quantifying the stability as a function of internal magnetizations can be used to inform the procedure to program these profiles in elastomagnetic swimmers.

Finally, although much of prior work has used numerical tools to identify conditions which result in locomotion, we would like to explore if there are underlying symmetries in the problem which give an intuitive reason behind the conditions that result in locomotion. For example, when the links have front back symmetry in magnetizations, identifying velocity symmetries in orientation dynamics provides an analytic way to reason about steady state solutions to the system without having to numerically simulate the dynamics. The hope is that by identifying structural symmetries in the dynamics, control inputs which exploit those symmetries can be designed.

References

[1] F Alouges, Antonio DeSimone, L Giraldi, and M Zoppello. Self-propulsion of slender micro-swimmers by curvature control: N-link swimmers. *International Journal of Non-Linear Mechanics*, 56:132–141, 2013.

[2] François Alouges, Antonio DeSimone, Laetitia Giraldi, and Marta Zoppello. Can magnetic multilayers propel artificial microswimmers mimicking sperm cells? *Soft Robotics*, 2(3):117–128, 2015.

[3] François Alouges, Antonio Desimone, Laetitia Giraldi, and Marta Zoppello. Purcell magneto-elastic swimmer controlled by an external magnetic field. *IFAC-PapersOnLine*, 50(1):4120–4125, 2017.

[4] Leif E Becker, Stephan A Koehler, and Howard A Stone. On self-propulsion of micro-machines at low reynolds number: Purcell's three-link swimmer. *Journal of fluid mechanics*, 490:15–35, 2003.

[5] M Belovs and A Cēbers. Ferromagnetic microswimmer. *Physical Review E*, 79(5):051503, 2009.

[6] Lisa Janelle Burton. *The dynamics and kinematics of bio-in swimming systems*. PhD thesis, Massachusetts Institute of Technology, 2013.

[7] Andrejs Cebers. Dynamics of a chain of magnetic particles connected with elastic linkers. *Journal of Physics: Condensed Matter*, 15(15):S1335, 2003.

[8] Andrejs Cebers and Kaspars Erglis. Flexible magnetic filaments and their applications. *Advanced Functional Materials*, 26(22):3783–3795, 2016.

[9] Sung Kwon Cho et al. Mini and micro propulsion for medical swimmers. *Micromachines*, 5(1):97–113, 2014.

[10] Giancarlo Cicconofri and Antonio DeSimone. Motion planning and motility maps for flagellar microswimmers. *The European Physical Journal E*, 39(7):72, 2016.

[11] RG Cox. The motion of long slender bodies in a viscous fluid part 1. general theory. *Journal of Fluid mechanics*, 44(4):791–810, 1970.

[12] Eric Diller, Jiang Zhuang, Guo Zhan Lum, Matthew R Edwards, and Metin Sitti. Continuously distributed magnetization profile for millimeter-scale elastomeric undulatory swimming. *Applied Physics Letters*, 104(17):174101, 2014.

[13] Rémi Dreyfus, Jean Baudry, Marcus L Roper, Marc Fermigier, Howard A Stone, and Jérôme Bibette. Microscopic artificial swimmers. *Nature*, 437(7060):862, 2005.

[14] Hermes Gadêlha. On the optimal shape of magnetic swimmers. *Regular and Chaotic Dynamics*, 18(1-2):75–84, 2013.

[15] Wei Gao, Daniel Kagan, On Shun Pak, Corbin Clawson, Susana Campuzano, Erdembileg Chuluun-Erdene, Erik Shipton, Eric E Fullerton, Liangfang Zhang, Eric Lauga, et al. Cargo-towing fuel-free magnetic nanoswimmers for targeted drug delivery. *small*, 8(3):460–467, 2012.

[16] Ambarish Ghosh and Peer Fischer. Controlled propulsion of artificial magnetic nanostructured propellers. *Nano letters*, 9(6):2243–2245, 2009.

[17] Chaohui Gong, Daniel I Goldman, and Howie Choset. Simplifying gait design via shape basis optimization.

[18] Emiliya Gutman and Yizhar Or. Simple model of a planar undulating magnetic microswimmer. *Physical Review E*, 90(1):013012, 2014.

[19] Emiliya Gutman and Yizhar Or. Optimizing an undulating magnetic microswimmer for cargo towing. *Physical Review E*, 93(6):063105, 2016.

[20] Emiliya Gutman and Yizhar Or. Symmetries and gaits for purcell's three-link microswimmer model. *IEEE Transactions on Robotics*, 32(1):53–69, 2016.

[21] Ross L Hatton and Howie Choset. Connection vector fields for underactuated systems. In *2008 2nd IEEE RAS & EMBS International Conference on Biomedical Robotics and Biomechatronics*, pages 451–456. IEEE, 2008.

[22] Ross L Hatton and Howie Choset. Approximating displacement with the body velocity integral. 2009.

[23] Ross L Hatton and Howie Choset. Geometric motion planning: The local connection, stokes' theorem, and the importance of coordinate choice. *The International Journal of Robotics Research*, 30(8):988–1014, 2011.

[24] Ross L Hatton and Howie Choset. Geometric swimming at low and high reynolds numbers. *IEEE Transactions on Robotics*, 29(3):615–624, 2013.

[25] Shigeo Hirose and Hiroya Yamada. Snake-like robots [tutorial]. *IEEE Robotics & Automation Magazine*, 16(1):88–98, 2009.

[26] T Honda, KI Arai, and K Ishiyama. Micro swimming mechanisms propelled by external magnetic fields. *IEEE Transactions on Magnetics*, 32(5):5085–5087, 1996.

[27] B Jang, E Gutman, N Stucki, BF Seitz, PD Wendel Garcia, T Newton, J Pokki, O Ergeneman, S Pane, Y Or, et al. Undulatory locomotion of magnetic multilink nanoswimmers. *Nano letters*, 15(7):4829, 2015.

[28] Scott D Kelly and Richard M Murray. Geometric phases and robotic locomotion. *Journal of Field Robotics*, 12(6):417–431, 1995.

[29] Islam SM Khalil, Herman C Dijkslag, Leon Abelmann, and Sarthak Misra. Magnetosperm: A microrobot that navigates using weak magnetic fields. *Applied Physics Letters*, 104(22):223701, 2014.

[30] A Koenig, Pascal Hebraud, C Gosse, R Dreyfus, J Baudry, E Bertrand, and J Bibette. Magnetic force probe for nanoscale biomolecules. *Physical review letters*, 95(12):128301, 2005.

[31] Jair Koiller, Kurt Ehlers, and Richard Montgomery. Problems and progress in microswimming. *Journal of Nonlinear Science*, 6(6):507–541, 1996.

[32] Eric Lauga. Theoretical models of low-reynolds-number locomotion. In *Fluid-Structure Interactions in Low-Reynolds-Number Flows*, pages 100–167. Royal Society of Chemistry, 2015.

[33] Juan B Melli, Clarence W Rowley, and Dzhelil S Rufat. Motion planning for an articulated body in a perfect planar fluid. *SIAM Journal on applied dynamical systems*, 5(4):650–669, 2006.

[34] Richard M Murray, Zexiang Li, S Shankar Sastry, and S Shankara Sastry. *A mathematical introduction to robotic manipulation*. CRC press, 1994.

[35] Richard M Murray and S Shankar Sastry. Nonholonomic motion planning: Steering using sinusoids. *IEEE Transactions on Automatic Control*, 38(5):700–716, 1993.

[36] Bradley J Nelson, Ioannis K Kaliakatsos, and Jake J Abbott. Microrobots for minimally invasive medicine. *Annual review of biomedical engineering*, 12:55–85, 2010.

[37] Jim Ostrowski and Joel Burdick. The geometric mechanics of undulatory robotic locomotion. *The international journal of robotics research*, 17(7):683–701, 1998.

[38] Kathrin E Peyer, Li Zhang, and Bradley J Nelson. Bio-inspired magnetic swimming microrobots for biomedical applications. *Nanoscale*, 5(4):1259–1272, 2013.

[39] Edward M Purcell. Life at low reynolds number. *Am. J. Phys*, 45(1):3–11, 1977.

[40] Edward M Purcell. Helmholtz coils revisited. *American Journal of Physics*, 57(1):18–22, 1989.

[41] Marcus Roper, Rémi Dreyfus, Jean Baudry, Marc Fermigier, Jérôme Bibette, and Howard A Stone. On the dynamics of magnetically driven elastic filaments. *Journal of Fluid Mechanics*, 554:167–190, 2006.

[42] Masahiko Sendoh, Kazushi Ishiyama, and K-I Arai. Fabrication of magnetic actuator for use in a capsule endoscope. *IEEE Transactions on Magnetics*, 39(5):3232–3234, 2003.

[43] Alfred Shapere and Frank Wilczek. Geometry of self-propulsion at low reynolds number. *Journal of Fluid Mechanics*, 198:557–585, 1989.

[44] Daniel Tam and Annete E Hosoi. Optimal stroke patterns for purcell's three-link swimmer. *Physical Review Letters*, 98(6):068105, 2007.

[45] Oren Wiezel and Yizhar Or. Optimization and small-amplitude analysis of purcell's three-link microswimmer model. *arXiv preprint arXiv:1603.02268*, 2016.